Title

Effectiveness of multi-stage cooling processes in improving the CH4-hydrate saturation uniformity in sandy laboratory samples

Authors

Yin, Zhenyuan
Moridis, George
Chong, Zheng Rong
et al.

Publication Date

2019-09-01

DOI

10.1016/j.apenergy.2019.05.077

Peer reviewed

Effectiveness of Multi-Stage Cooling Processes in Improving the CH_4-Hydrate Saturation Uniformity in Sandy Laboratory Samples[1]

Zhenyuan Yin[a,b], George Moridis[c,d,a], Zheng Rong Chong[a], and Praveen Linga[a]*

[a] Department of Chemical and Biomolecular Engineering, National University of Singapore, S117585, Singapore

[b] Lloyd's Register Singapore Pte. Ltd., S138522, Singapore

[c] Petroleum Engineering Department, Texas A&M University, TX 77843, USA

[d] Earth Sciences Division, Lawrence Berkeley National laboratory, CA 94720, USA

Abstract

Laboratory-created samples of methane hydrate (MH)-bearing media are a necessity because of the rarity and difficulty of obtaining naturally-occurring samples. The hypothesis that the inevitable heterogeneity in the phase saturations of the laboratory samples may lead to unreliable and non-repeatable results provided the impetus for this study, which aimed to determine the conditions under which maximum uniformity can be achieved. To that end, we designed four experiments involving different multi-stage cooling regimes (in terms of their duration and number of stages) to induce MH formation under excess-water conditions. In the absence of direct visualization capabilities, we analysed the experimental results by means of numerical simulation, which provided high-resolution predictions of the spatial distributions of the phase saturations in the cores and enabled the estimation of the parameters controlling the kinetic MH-formation behaviour through history-matching. Analysis of the numerical results indicated that, under the conditions of the experiments and with the design of the reactor, significant heterogeneities in phase saturation distributions were observed in all cases, leading to the conclusion that it is not possible to obtain cores with uniform phase saturation. Additionally, contrary to expectations, heterogeneities increased with the number of cooling stages and the duration of cooling, and this was attributed to imperfect insulation of the upper part of the reactor. A set of simulations involving perfect insulation of the reactor top confirmed the validity of this assumption: (a) predicting the formation of high-uniformity MH-bearing cores that became more homogeneous as

[1] The short version of the paper was presented at ICAE2018, Aug 22-25 (2018), Hong Kong. This paper is a substantial extension of the short version of the conference paper.

the number of cooling stages and the length of the cooling period increased; and (b) providing important information for the improvement of the standard design of the experimental apparatus for the laboratory creation of MH-bearing cores using the excess water method.

Keywords: methane hydrate; hydrate formation; cooling process; kinetic rate; heterogeneous phase distribution

*Corresponding author(s): P. Linga (praveen.linga@nus.edu.sg); G. Moridis (gjmoridis@lbl.gov)

1. Introduction

Methane hydrates (MHs) are being considered as a future source of energy due to the abundance of the resource volume in nature and their ability to store large amounts of CH_4 (1 m^3 MH store up to 172 m^3 of CH_4 under *STP*) [1]. The current resource estimation of the gas-in-place for hydrate bearing sediment (HBS) worldwide is 3,000-20,000 trillion cubic meter (TCM) [2], which easily surpasses the global reserve of natural gas (~193.5 TCM [3]) in 2017. Nearly 99 % of the gas stored in hydrate form is assessed to be at marine (offshore) locations, and the remaining 1 % involves onshore deposits associated with the permafrost [4]. The possible recovery of CH_4 from deposits in sediments for energy has being attracting ever-increasing interest in several countries, e.g. U.S.A, Japan, India, China, Norway and South Korea. Two most recent field tests carried out in 2017 at Japan Eastern Nankai Trough [5] and South China Sea Shenhu Area [6] provided evidence in support of the long-term economic-viable production of CH_4 from hydrate accumulations in the near future.

To recover CH_4 for energy from geological hydrate reservoirs, it is important to have a thorough understanding on the mechanisms of hydrate formation and dissociation in porous media. This requires knowledge gleaned from studies at different scales, i.e., at pore- [7-9], core- [10, 11] and reservoir-scale [12, 13]. The examination of hydrate cores under laboratory conditions provides insights into the hydrate growth habits, the thermophysical properties of the hydrate-medium complex system, and of the overall behaviour during formation/dissociation, all critical in understanding and designing the production process [14]. The importance of these laboratory tests cannot be over-emphasized, but such studies are severely hampered by the difficulty of forming/procuring samples representative of hydrate-bearing media under field conditions [15]. The very small number of field studies (a total of eight since energy recovery emerged as a possibility), the difficulty of conducting such studies under the hostile conditions of hydrate occurrence in natural deposits [16], and the instability of hydrates during the short period between core recovery and storage (caused by their sensitivity to pressure and temperature changes [17]) are the reasons for the rather extreme scarcity of natural hydrate-bearing cores that are representative of field conditions. This being the case, laboratory-created hydrate-bearing samples are probably the only possible option despite questions about their representativeness of field conditions.

Creation of hydrate-bearing cores in the laboratory and analysis of their formation and dissociation behaviour is fundamentally challenging because of the difference in the boundary conditions, and the temporal and spatial scales between the reactor and the geological reservoir [18]. Despite these shortcomings, studies on lab cores are valuable because the physics involved in hydrate formation in porous media is convoluted and may not be fully elucidated so far, as they involve complex coupled processes that include gas dissolution, hydrate nucleation and growth kinetics, fluid and heat flow through the porous medium, as well as other physical and chemical interactions between fluids, hydrate and the host sediment [18, 19].

To date, various techniques have been devised to form hydrate in porous media in the laboratory, including the excess-gas method [20, 21], the excess-water method [22, 23], the dissolved-gas method [24] and the ice-to-hydrate method [25]. A persistent and recurring issue in all these techniques is that of spatial heterogeneity of hydrate in the core [15, 20, 24, 26]. This has the potential to be a serious fundamental issue because the thermophysical and geomechanical properties of HBS, as well as the production behaviour exhibited during laboratory experiments, can be substantially different if HBS is treated as a spatially heterogeneous system rather than a commonly-assumed homogeneous material [26]. The problem of spatial heterogeneity can be overcome if visual observations of its distribution (e.g., obtained from X-Ray computer tomography (CT) scans during the formation/ dissociation process) are available and are coupled with numerical simulation [27], but such facilities are not widely available. This leads to concerns about the reliability of conclusions drawn from studies based on the assumption of homogeneity without any supporting evidence.

At core-scale, Kneafsey et al. [28] performed a series of hydrate formation experiments that were monitored with X-ray CT scanning, aiming to quantify the spatial distribution of localized differentials in density change (a measure of heterogeneity) during MH formation. Their observation that the S_H distribution was spatially heterogeneous in all experiments was attributed to differences in the localized heat transfer and in the water migration due to capillary. Based on the X-ray CT scanning results, the composite thermal conductivity model of a heterogeneous porous methane hydrate sample was further determined by Gupta. et al [26]. Linga et al. [20] conducted experiments to investigate the MH formation in unconsolidated silica sand and also reported the occurrence of persistent spatial heterogeneity, as indicated by the response of

thermocouples at different locations within the core. The laboratory study of Rees et al. [29] provided further evidence of heterogeneity during MH formation in cores, with their results suggesting that hydrate preferentially grows in areas of low initial water saturation. Besides X-ray CT scanning, magnetic resonance imaging (MRI) [30, 31] and electrical resistivity tomography [32] have also been applied in the visualization of the phase distribution during MH formation and dissociation processes. All studies consistently point out to a non-uniform S_H in the laboratory cores despite the difference in the size of the reactor and the MH formation method.

The numerical studies of Yin et al. [33, 34] analysed through history-matching (inverse modelling) laboratory data of MH formation and dissociation in a sandy core in a 1.0 L reactor, and the optimized parameters determined in the process closely matched the pressure and temperature measurements and yielded consistent predictions of heterogeneous spatial distributions of all phases. The MH formation method of Chong et al. [23, 35] that provided the data for the Yin et al. [33, 34] studies was shown to lead to significantly heterogeneous spatial distributions of S_H (high S_H near the reactor cooling boundary, and low S_H at the reactor centre) as a result of the apparatus design. The numerical studies of Yin et al. [33, 34] also determined that the thermal processes associated with the reactor cooling and the warm water injection (to effect dissociation) had a considerable impact on the spatial distribution of S_H in the hydrate-bearing core, as did the ambient air temperature.

For studies without the benefit of in-situ phase visualization, numerical predictions of the hydrate distribution in the sample and of its behaviour during dissociation are the only means of addressing the issue of heterogeneity [33, 34, 36]. Numerical simulation can address the complexity of the various intertwined physical and chemical processes during hydrate formation and dissociation. However, based on the drastically different evolution of the spatial distributions of hydrate saturation (S_H) in uniform and heterogeneous samples during dissociation reported in earlier studies [34, 36], a reasonable assumption is that the addition of the complexity of spatial heterogeneity may lead to potentially significantly different results, thus increasing the uncertainty about the reliability of the numerical predictions of the system behaviour. Consequently, reducing the uncertainty of spatial heterogeneity in the laboratory-created samples (i.e., by creating and working with more homogeneous samples) is desirable, as the underlying hypothesis is that it is expected to lead to more reliable conclusions about the hydrate system behaviour. The current

study aims to investigate the possibility of creating spatially homogeneous samples using a specific technique (excess-water), and the conditions under which this may be likely or even feasible.

Most laboratory studies of core behaviour up to now have only focused on the morphology and the characteristics of fluid flow during MH formation [37-39], and far fewer have addressed the heat transport behaviour and the kinetics of the hydrate formation reaction in cores. Practically all hydrate formation studies have been conducted by either exposing the core-containing vessel to a constant low temperature [20, 29] or by rapid cooling of the vessel in a step that lowers the temperature below the equilibrium level [23, 35, 40]. There is limited information on the system behaviour and the phase spatial distributions induced by a different cooling process (e.g., slow cooling rate and low degree of sub-cooling). Jiang et al. [41] studied the effect of cooling rate on the MH nucleation time and on the CH_4 conversion rate but only qualitatively, with no effort to quantify/correlate the various processes. Zhang et al. [42] investigated the influence of varying temperatures during MH formation in water (i.e., in the absence of a porous medium) and the associated gas consumption under a constant pressure mode, but the applicability of his results to core studies is questionable. More recently, the effect of sub-cooling on the formation of natural gas hydrate was investigated by Mali et al. [43], but their work focused on nucleation (i.e., on the evolution) of hydrates, did not consider any later-time hydrate behaviour and its kinetics and did not involve a porous medium, making it practically irrelevant to core studies.

Gleaning from our past experience with both experiments and simulations of the MH formation process in sandy media [20, 23, 33], we postulate that the rate of hydrate formation rate (and the corresponding heterogeneity effects on the spatial distribution of S_H) can be controlled by the degree of sub-cooling (ΔT_{sub}) applied to the closed system (laboratory apparatus) used in the excess-water method. The term ΔT_{sub} can be defined as the onset temperature of MH below its equilibrium temperature (T_{eq}). We hypothesize that slowing down the rate of formation in a series of intermediate sub-cooling steps toward the final temperature set point can lead to more uniform phase distributions (including that of S_H) in the core. To validate this hypothesis, we designed and executed four sets of laboratory experiments in a V = 1.0 L reactor that involved the formation of hydrates under four different cooling regimes. We then (a) analysed the results of the laboratory studies by means of numerical simulation and a history-matching process that determined the values of the parameters controlling the formation process through minimization of the differences

between laboratory measurements and numerical predictions [29], and (b) estimated the associated phase distributions in the cores and the levels of heterogeneity. The study also discusses the possible controlling mechanisms that can explain the behaviour of hydrate formation at preferential locations in the sandy medium and the possible method to improve the homogeneity of the sample.

2. Experimental Section

2.1 Experimental Apparatus

Fig. 1a shows the schematic of the experimental apparatus used for the MH formation experiments. The key component consists of a reactor, which is a cylindrical pressure vessel (D_{in} = 102.0 mm; H = 120.0 mm) made of stainless steel 316 (SS316). The thickness of the reactor wall is 15.0 mm and the thickness of the top and bottom flange is 25.0 mm. The reactor volume is V = 0.98 L. The reactor is surrounded by a temperature-controlled circulating water bath, the temperature of which is controlled by a 15.0 L external refrigerated circulator (model SD15R-30, PolyScience). The reactor and the circulating water line are wrapped with insulation foam to prevent heat exchange with its surroundings. A syringe pump (model 500D, Teledyne ISCO) is used for water injection through valve V_2 during MH formation. The temperature of the injected water is controlled by a 7.0 L external refrigerated circulator (model SD07R-20, PolyScience). Three Rosemount Smart pressure transmitters (± 20.0 kPa) are used for pressure measurements of the reactor at locations of P_{top}, P_{bot} in Fig.1a. Two copper-constantan six-point T-type thermocouples (± 0.1 K) are installed at the locations T_a and T_b (see Fig. 1b). Two single-point thermocouples are located in the water bath (RC1) and at the water injection nozzle (V_8). Table 1 lists the different type of the temperature and pressure sensors used in this study with their location and accuracy. The data acquisition system (National Instruments) records the experimental data using the LabView 2017 (National Instruments) software. The reactor is also equipped with a pressure relief valve for safety purposes. All the tubes of the experimental apparatus are stainless steel tubing (d_{in} = 4.6 mm) from Swagelok.

2.2 Experimental Materials

Methane gas of 99.9% purity (Air Liquid Singapore Pte. Ltd.), silica sand with an average diameter of 212 μm (diameter ranges from 100 to 520 μm – see Fig. 2a) and deionized water are used for the experiments. The density of the sand is 2.65 g/cm^3. Mercury porosimetry analysis of the sand

yielded an average pore diameter of 21.9 μm with a BET surface area of 230 m^2/g. The porosity and permeability of the sand are ϕ = 44.6% and k = 3.83 darcys, respectively. The relationship between the capillary pressure of the porous medium and the water saturation is shown in Fig. 2b, and is described by the model of van-Genuchten (vG) [44] with the parameters summarized in Table 2. Differential calorimetry scanning (DSC) test of the dry sand provided an estimate of the specific heat capacity of the sand as C_R = 800 J/(g °C). All the thermophysical properties of the sandy medium discussed above were applied in the numerical simulation section of this study.

2.3 Experimental Procedure

2.3.1 Methane hydrate formation

The amount of silica sand that was tightly packed in the reactor for each experiment was 1480.5 g. The height of the sand bed was 120.0 mm, which completely covered the height of the reactor. Prior to the execution of the experiments, the reactor was sealed and purged three times with CH_4 gas at a pressure of 1.0 MPa to remove the initial/residual air. A fixed amount of CH_4 gas was then slowly injected into the reactor at a rate of Q_G = 0.1 kPa/s to pressurize the system to final conditions of P = 6.5 MPa at T = 15.0 ºC (corresponding to $\boldsymbol{n}_{CH4}$ = 1.32 mol inside the reactor). Deionized water was then injected into the reactor at a rate of Q_W = 50 ml/min for t = 3.5 min to further pressurize the system to P = 9.6 MPa. The volume of the water injected into the system in each experiment is summarized in Table 3. The system was then left to rest for t = 90.0 minutes, thus allowing the gas and the aqueous phase to redistribute and stabilize inside the reactor to initial phase saturations of S_A = ~0.4 and S_G = ~0.6 (see Table 3). Given that the ratio of the injected amount of water to gas ($\boldsymbol{n}_{H2O}/\boldsymbol{n}_{CH4}$ = 7.32) was larger than the typical hydration number (N_H = 6.0), the experimental conditions for the MH formation can be considered to reflect an excess-water environment.

As already explained, one of the hypotheses to be tested by these experiments is that increased homogeneity is desirable as it is expected to provide more reliable results. In working toward the goal of creating more homogeneous hydrate-bearing core samples, we made the assumption that a longer cooling process may lead to increased homogeneity and designed accordingly four experiments. The procedure for the injection of gas and water was the same for all the experiments. The hydrate formation was induced by four different multi-stage cooling regimes that are depicted in the schematic of Fig. 3a. The four different cooling processes in our experiments are described

by the *P*-*T* trajectory during the MH formation (in relation to the P_{eq}-T_{eq} equilibrium curve) shown in Fig. 3b. Experiment C1 involved a single-stage cooling process, in which the system is cooled down from 15.0 ºC to 0.8 ºC. Experiments C2 and C3 involved a 2-stage (15.0 ºC to 8.0 ºC to 0.8 ºC) and a 3-stage (15.0 ºC to 10.0 ºC to 5.0 ºC to 0.8 ºC) cooling process, respectively. Experiment C4 comprised the largest number - 12 cooling steps from 15.0 ºC to 0.8 ºC and had the longest MH formation time (t = 300.0 hr). The variations in P and T during each cooling step were caused mainly by the MH formation (and, to some extent, to the heat exchange with the reactor surroundings because perfect insulation is practically impossible) and were constantly monitored, as they provided the necessary data for the history-matching process and the deduction of the key parameters describing the system behaviour. Each step was sufficiently long to allow practical stabilization of both the pressure and temperature in the reactor.

2.4 Estimation of the average phase saturations

The average phase saturations of the various phases (S_A, S_H and S_G) were estimated based on the volume balance of the pore-space. Key assumptions of this approach are that (a) the porosity of the sandy medium (φ) does not change with time and (b) pressure variations have a minimal effect on φ. These are valid assumptions under the conditions of the experiment. The pore volume is occupied by three phases during MH formation, namely the gas phase (G), the aqueous phase (A) and the MH phase (H). Note that the amount of CH_4 dissolved in the aqueous phase is less than 1.0 % of the total amount of CH_4 injected into the reactor because of its low solubility (0.065 mol/kg H_2O at 1.2 ºC [45]) and will not be considered in the pore-volume-based estimates. The advantage of this method over the classical gas-uptake method is that the volume change of the gas phase during the MH formation in sandy medium is fully accounted for. A comparison between the estimates of S_H over time from these two different methods is shown in Fig. S1 in the supporting information section of this paper.

The reaction of MH formation is described by

$$CH_4 + N_H H_2O \rightleftarrows CH_4 \bullet N_H H_2O \quad (1)$$

in which the average hydration number is assumed to be N_H = 6.0 [46]. The pore-volume balance equation is described by

$$V_{pore} = V_r \times \phi = V_{gas} + V_{water} + V_{MH} = n_{gas}\rho_{gas} + n_{water}\rho_{water} + n_{MH}\rho_{MH} \quad (2)$$

in which n_i (mol) represents the number of mole and ρ_i (cm^3/mol) represents the molar density of the i^{th} phase. The terms n_i can be further expressed as

$$n_{gas} = n_{gas,init}(1 - x_{gas}) \quad (3)$$

$$n_{water} = n_{water,init} - N_H \times x_{gas} \times n_{gas,init} \quad (4)$$

$$n_{MH} = x_{gas} \times n_{gas,init} \quad (5)$$

and represent the initial amount of gas and water injected, less the amount consumed during the MH formation reaction. The term x_{gas} represents the conversation of CH_4 gas into MH.

The molar densities of the aqueous phase and of the MH phase have the constant values of 18.0 cm^3/mol and 136.7 cm^3/mol, respectively, because the effect of temperature and pressure on them is not significant [47]. The molar density of the gas phase (100% CH_4) is estimated based on the measured P and T of the reactor using the Peng-Robinson equation of state because of the non-ideality of CH_4 under high pressure (3.0 MPa $< P <$ 10.0 MPa). Thus, by combing Eqn. (2)-(5), we can estimate the conversion of CH_4 to MH through the continuous measurements of the P and T in the reactor during MH formation and the use of a numerical tool (MATLAB R2018b in this study) that solves the coupled equations. The saturation of each phase in the reactor is then estimated based on the volume fraction of each phase as

$$S_i = V_i / V_{pore} = n_i \rho_i / V_{pore} \quad (6)$$

Note that the phase saturation estimated based on this method is only representative of the phase saturations in the reactor, with no consideration of its spatial distribution. The spatial distribution of the various phases can be determined by state-of-the-art instrumental techniques (e.g., X-ray CT scanning [15, 27], MRI [48], Electrical Resistivity Tomography (ERT) [32], etc.) that provide direct visualization data. In the absence of such specialized equipment (as is our case), the only option is the use of a numerical simulator that accounts for all physics involved in the hydration/dissociation processes and is provided with a fine spatial discretization of the detailed geometry of the reactor.

3. The Numerical Model and the Simulation Approach

3.1 The T+H numerical model and the kinetic rate model

The simulations in this study were conducted using the T+H code [49, 50] , a numerical simulator developed at the Lawrence Berkeley National Laboratory (LBNL) to model the CH_4-hydrate behaviour during formation and/or dissociation under any conditions of occurrence of CH_4-hydrates (i.e., in the permafrost and in deep ocean sediments, as well in any laboratory experimental set-up) by solving the coupled equations of mass and heat balance associated with such systems. The simulator can model all the known processes involved in the system response of CH_4-hydrates in complex geologic media, including the flow of fluids and heat, the thermophysical properties of reservoir fluids, the thermodynamic changes and phase behaviour, and the non-isothermal chemical reaction of CH_4-hydrate formation and/or dissociation, which can be described by an equilibrium model [36] or a kinetic model [33]. T+H is a fully implicit compositional simulator, and its formulation accounts for heat and the various mass components that are partitioned among four possible phases: *G*, *A*, *H*, ice (*I*). It can handle the phase changes, state transitions, strong nonlinearities and steep solution surfaces that are typical of hydrate formation and dissociation problems. A detailed description of the code, its underlying physics and capabilities of the numerical techniques can be found in Moridis [49, 50].

3.2 Simulation domain and discretization

The grid used in the simulation component of this study was the same used in the earlier work of Yin et al. [33, 34], as the same reactor was used in the experiments of both studies. The 2D axisymmetric cylindrical grid (see Fig. 4) had been constructed using the MeshMaker v1.5 application [51] and accurately represented the geometry of the hydrate reactor (see Fig. 1b). For maximum accuracy and for reasons discussed in Yin et al. [33, 34], a very fine spatial discretization was used to subdivide the domain. The interior of the reactor (with a radius r = 51.0 mm) was discretized into 29 subdivisions (5 × Δr = 0.6 mm and 24 × Δr = 2.0 mm), and the reactor wall thickness (d_{wall} = 15.0 mm) was discretized into 5 uniformly-sized subdivisions (5 × Δr = 3.0 mm) in order to accurately capture the transport of heat between the interior of the reactor and the circulating water. The radius of the water injection nozzle is 2.4 mm and is described using four elements (4×Δr = 0.6 mm) located at the top center of the reactor. One additional outermost subdivision (Δr = 0.1 mm) was added to describe the time-dependent temperature boundary of the

circulating water (marked as blue in Fig. 4). The internal height of the reactor (h = 120.0 mm) is discretized into 48 uniformly-sized subdivisions in z (Δz = 2.5 mm). In addition, the thickness of the top and bottom flange of the reactor (d_{top} = d_{bot} = 25.0 mm) was discretized into 5 uniform subdivisions (5 × Δz = 5.0 mm), with one additional uppermost layer (Δz = 0.1 mm) depicting the ambient (constant-temperature) air boundary (marked as red in Fig. 4).

In total, the cylindrical simulation domain was discretized into 35 × 59 = 2065 elements in (r, z). The fine discretization is important in the effort for accurate predictions in the small reactor system [23], as it is necessary to capture the hydrate formation fronts and the dynamic heat and flow behavior expected near the injection nozzle. With no inhibitors (such as salt) in the system, the domain discretization resulted in a total of 8260 simultaneous equations to be solved at each time step under the assumption of a kinetic hydrate formation reaction.

3.3 System thermophysical properties and boundary conditions

Table 2 summarizes the key thermophysical properties of the fine quartz sand used in the experiment. The composite thermal conductivity model of MH-bearing sediment in this study was estimated using the linear composite model [49], which accounts for all three phases. In the absence of direct measurements, the parameter values of Table 2 that are associated with the relative permeability [52] were representative of sandy materials. The kinetic equation of hydrate formation follows the Kim-Bishnoi [53] and the Clarke and Bishnoi models [54]. In Table 2, the values of the parameters of the surface area adjustment factor F_A are those evaluated through a history-matching technique [55] that minimizes the deviations between the experimental data and the numerical predictions in P and T [33]. The temperature of the circulating water that induced hydrate formation in all four cases is shown in Figs. 5 and 6, and were implemented as boundary conditions in the simulations.

4. Results and Discussion

4.1 General behaviour of MH formation induced by multi-stage cooling

Fig. 5 shows the trajectory of the measured P_{avg} (average P of P_{top} and P_{bot}) and T_{avg} (average T of all the twelve T-monitoring points) during the MH formation experiments in relation to the MH P_{eq}-T_{eq} equilibrium curve. In all cases, the pressure decreases linearly as the temperature decreases from T = 17.0 °C to 12.4 °C (outside the MH stability zone) mainly because of gas dissolution and

cooling. MH does not form immediately when the *P*-*T* first move outside the MH stability zone because of metastability (i.e., the ability of a non-equilibrium state to persist for a long period of time [1]). The onset of MH formation occurs at a temperature lower than T_{eq} at the prevailing pressure, and this temperature decreases as the number of cooling steps decrease (as expected). In addition, the temperature decline during the MH formation is not linear toward the set-point of each cooling step, but the P_{avg}-T_{avg} curve exhibits a wavy pattern. This is caused by the rapid hydrate formation, which releases a large amount of latent heat that cannot be removed sufficiently fast by the circulating cooling water. In all the cooling steps, the final *P* coincides with the equilibrium P_{eq} of MH at the set point *T* (see Fig. 5).

Fig. 6 shows the evolution of pressure (P_{top} and P_{bot}) and temperature (T_{a4}, T_{b4} and T_w) over time in the four experiments. In all experiments, the MH formation in the sandy core involves three stages: (a) gas dissolution; (b) primary formation and rapid growth; and (c) slow growth coupled with secondary formation (see discussion in the next section). In experiment C1 (a typical single-stage cooling process), the time before the onset of hydrate formation (which is indicated by a rapid temperature increase − see the temperature peak in Fig. 6a) is characterized by a linear decline of *P* (from *P* = 9.5 MPa to *P* = 9.2 MPa) and *T* (from *T* = 16.0 °C to *T* = 6.0 °C) because of CH_4 dissolution and the effect of the cooling boundary. Hydrate formation is marked by a rapid temperature increase (marked by the temperature peak in Fig. 6a) and a fast pressure drop. The decrease of pressure (caused by the uneven CH_4 consumption – as affected by the changing active area of formation – and the continuing heat loss to the cooling boundary) over time is not linear. Note that the temperature response is faster than that of the pressure.

We observed a similar behaviour of *T* and *P* in experiments C2-C4, as shown in Figs. 6b-6d. In these cases, the time available for MH formation was significantly longer as the number of the cooling steps increased from *t* = 11.0 hr in experiment C1 to *t* = 300.0 hr in experiment C4. Another important observation from Fig. 6 is that the temperature inside the reactor does not converge (as expected) to that of the circulating water bath, but a small deviation (~1.0 °C) persists in all cases. This is attributed to the imperfect insulation of the upper part of the reactor which would allow heat inflow from the boundary, but also (to a lesser degree) to continuing low-level MH formation − as indicated by the continuing downward trend of the pressure after the end of the last cooling step.

4.2 Effect of multi-stage cooling on MH formation in sandy medium

Primary formation events were observed in experiments C1 to C3 during each cooling step (see Fig. 6). C4 was an exception because of the small boundary temperature drop (1 ºC) and the more efficient heat removal at each of the longer cooling steps. In experiment C1, the temperature exhibited a sharp peak at t = 1.0 hr, increasing rapidly from initial T_{init} = 6.0 ºC to T_{peak} = 8.0 ºC (T_{peak} = 2.0 ºC) (see Fig. 6a) and suggesting fast hydrate formation and a corresponding release of latent het that cannot be removed rapidly through the cooling boundaries. Multiple secondary formation events were also observed with temperature peaks occurring between t = 7.0-10.0 hr. The same behaviour indicative of both primary and secondary formation is obvious in experiments C2 and C3 (see Figs. 6b and 6c).

The magnitude of the temperature peak (T_{peak}) associated with the primary MH formation decreases with the level of sub-cooling (related to the number of the cooling steps and quantified by the ΔT_{sub}). Thus, T_{peak} increases from 0.3 ºC (ΔT_{sub} = 2.0 ºC, in experiment C3) to T_{peak} = 1.5 ºC (ΔT_{sub} = 4.0 ºC, in experiment C2) and to T_{peak} = 2.0 ºC (ΔT_{sub} = 11.0 ºC, in experiment C1). This observation holds true at all the twelve thermocouple positions, and is shown in Fig. S2-S5 in the supporting information section of this paper.

It is evident from Fig. 6 that secondary formation events, which are marked by a short temperature peak in a short duration, are less significant than the primary formation events. However, they are observed at multiple times in experiments C1 to C3. Such secondary MH formation can generate new surface area for hydrate formation and enhance the hydrate growth rate, as is evidenced by the faster pressure drop after secondary MH formation. It should be noted though that the time and extent of secondary MH formation are generally unpredictable.

The time between the system first entering the MH stability zone (P = 9.2 MPa and T = 12.4 ºC) and the emergence of the first clearly discernible temperature peak is defined as the induction time (t_{ind}) in our study. Table 3 lists the t_{ind} for experiments C1 to C3 (C4 does not show discernible peaks), which lead to the conclusion that stronger sub-cooling shortens the induction time for hydrate formation. To explain these observations, we used the classical nucleation theory (as nucleation is the basis of MH formation) and define the supersaturation ratio of the system (S) as:

$$S = \frac{c_A}{c_{AH}} - 1 \quad (7)$$

where c_A (mol/kg) is the CH_4 solubility in aqueous phase and $_{CAH}$ (mol/kg) is the CH_4 solubility in aqueous-hydrate equilibrium phase (see Fig. 7a). The S in experiments C1, C2 and C3 are S = 2.4, 0.9 and 0.6, respectively. Before the onset of formation, dissolution of CH_4 into water will be the dominant process. Hydrate nucleation in sandy medium is considered a heterogeneous process, with impurities acting as accelerators. The rate of nucleation (which gives the measure of MH formation), J (nuclei/m^3/s) is expressed in the form of an Arrhenius-type reaction equation [56] as

$$J = A\exp[\frac{-16\varphi\pi\gamma^3 v^2}{3k^3T^3(\ln S)^2}] \quad (8)$$

where A (nuclei/m^3/s) is the model constant, k (J/K) is the Boltzmann constant, γ (J/m^2) is the interfacial tension, v (m^3) is the molecular volume of the MH and φ is the adjustment factor for heterogeneous nucleation. This equation indicates that three main variables govern the rate of formation: temperature, T; supersaturation, S; and the interfacial tension, γ. From Eq. (2), it can be further shown that J increases exponentially with S [56]. The higher the S, the higher the J and the larger the latent heat release per unit time. This explains the decreasing T_{peak} as the number of steps increase from experiment C1 to C3.

Following the approach of Natarajan et al. [57], the t_{ind} and S are related through the following power function:

$$t_{ind} = k \times S^{-m} \quad (9)$$

where k and m are empirical parameters. In this study, the best fitted model parameters are k = 4992 s and m = 0.4154 for CH_4-hydrate, and the fitted curve is shown in Fig. 7b.

4.3 The evolution of average phase saturations over time

Fig. 8 shows the evolution of the average phase saturations over time for all three phases (S_H, S_A and S_G) estimated using the pore-volume balance method that we discussed in Section 2.4. Fig. 8a shows that the rate of the increase of S_H reflects the rate of the heat removal, which is determined by the number of cooling steps and the overall duration of the four experiments. Thus, the estimated average growth rate of S_H is Q_{SH} = 2.7%/hr, 2.3%/hr, 1.0%/hr, and 0.1%/hr in

experiments C1-C4, respectively. The step-wise pattern of the increase in S_H reflects the number of the cooling steps. The Kim et al. [53] and the Clarke and Bishnoi [54] model describes the kinetic rate of hydrate formation/dissociation as

$$n_H = K \exp(\frac{-\Delta E}{RT}) A_S (f_g - f_{eq}) \quad (10)$$

where K (mol/m^2 Pa s) is the MH formation reaction rate constant, ΔE (kJ/mol) is the activation energy, A_S (m^2) is the hydrate formation reaction surface area; f_g (Pa) and f_{eq} (Pa) are the fugacity of the CH_4 in gas phase and in hydrate equilibrium phase. The driving force for MH formation is considered as the fugacity difference $\Delta f = f_g - f_{eq}$, and the larger the Δf, the larger the rate of hydrate formation. Consequently, the strong sub-cooling in Case C1 (ΔT_{sub} = 11.0 ºC, the largest of all cases) is expected to lead to the highest Q_{SH}. Experiments C2 to C4, which involved progressively smaller ΔT_{sub} and Δf as the number of cooling steps increased, were expected to result in correspondingly smaller formation rates.

The results of the experiment confirm these expectations. The final S_H's in all experiments are very similar at the 0.31 level (see Table 3), and this realization conforms to expectations as the experiments involved the same stoichiometry of CH_4 and H_2O.

As expected, the average S_G and S_A in Figs. 8b and 8c decreased over from their initial levels (as CH_4 and H_2O were consumed during the hydrate formation) and the decrease followed a pattern that was a mirror image (opposite trend) of that of the S_H. The effect of the hydrate formation on S_G is much less significant than that of S_A: S_A decreased by 62.5% from S_A = 0.40 to 0.15 (see Fig. 8b), whereas S_G decreased by 10.0 % from S_G = 0.60 to 0.54 (see Fig. 8c). This is a direct consequence of the hydration number of MH (N_H = 6.0).

Theoretically, when P and T reach their final levels, they coincide with P_{eq} and T_{eq} and the system is stabilized in a state of coexistence of all three phase (A, G and H) as there is no driving force to effect further hydrate formation. In reality, P approach asymptotically to P_{eq} and some residual hydrate formation persist, albeit at extremely low levels. This can be discerned from the evolution of P in Fig. 6, which does not show evidence of complete stabilization even as the temperature is stabilized. Note that there is experimental evidence of this behaviour [20]. The final phase saturations in all experiments were practically identical at S_H = 0.31, S_A = 0.15 and S_G = 0.54.

4.4 Evolution of key variables and optimized numerical predictions

4.4.1 Initial spatial distribution of P, T, S_H, S_A and S_G

In the absence of direct visualization capabilities, numerical simulation is the only option to estimate the spatial distribution of various phases in the reactor during all stages of the experiments. This was accomplished by using the T+H simulator [49] in an approach that followed closely that of Yin et al. [33, 34]. In the kinetic model option of the simulator, the quantification of the surface adjustment factor term (F_A) can be one of the most challenging tasks in analysing experimental results of MH behaviour in sandy media [33, 40, 58]. Yin et al. [33, 34] provided a detailed description of the estimation of F_A by means of history-matching. In this study, we determined the optimal value of F_A that minimized the difference between the simulated and experimental measured P and T. The optimized F_A was used in the numerical study that provided the spatial distributions of various phases in the four experiments.

The preparatory steps of water injection, phase redistribution and stabilization have been discussed in the study of Yin et al. [33] and will not be repeated here as they were the same in this study. Figs. S6 and S7 in the supplementary information present the evolution of P and T and show a very good agreement with the experimental observations during the preparatory phase of the experiments. The numerically-predicted spatial distributions of P, T, S_A and S_G at the end of these two steps are shown in Fig. S8 and S9, respectively. The initial saturations before the hydrate formation were S_A = 60.0 % at the bottom of the reactor and S_G = 70.0 % at the top (see Fig. S9), and were used as the initial conditions in the subsequent simulations of all the cooling experiments.

4.4.2 Results in Case C1

Fig. 9 shows the simulation results of the evolution of P, T, and of the saturations and mass of all phases in Case C1. The simulated P and T are in excellent agreement with the experimental measurements (Figs. 9a and 9b). The temperature peak that is associated with the rapid primary hydrate formation at t = 1.5 hr is captured by the simulation (see Fig. 9b), although there is some attenuation of the numerical signal. This temperature peak is related to the transition from localized fast rate of MH formation to a slower phase of formation in the entire reactor volume (indicative of the bulk of primary MH formation) and is reflected by the decrease in the value of F_A (and, consequently, of the surface area) at that time (see Table 4). The evolution of the mass of the various phases in Fig. 9c clearly marks the early (localized and rapid) hydrate formation and the

transition into the slower, volume-wide formation by the large change in the slope of the associated curves. This is also reflected in the evolution of the phase saturations in Fig. 9d. The numerical predictions of the phase saturations are in good agreement with the estimates obtained from the pore-volume balance method (see Fig. 8).

4.4.3 Results in Cases C2 to C4

The numerical analysis of the experimental results in Cases C2 to C4 followed the same approach discussed in Case C1, and the associated optimized F_A values are listed in Table 4. The evolution of *P*, *T*, the mass and the saturation of the various phases are presented in Figs. 10 to 12, and show an excellent match between the simulation predictions and the experimental measurements. In all cases, the values of the optimized F_A decreased from the beginning to the end of the experiments by about an order of magnitude (from 10^{-1} to 10^{-2}), with occasional increases in-between (to be discussed later).

As in the C1 case, the simulator captures (albeit in an attenuated mode) the temperature peaks that now are associated with not only the formation transition (indicative of the bulk of the primary MH formation), but also of the secondary MH formation. The first abrupt change in the slope of the curves of the phase masses (Figs. 10c and 11c for Cases C2 and C3, respectively) and of the saturations (Figs. 10d and 11d) marks the onset of the volume-wide primary MH formation and is followed by a linear increase until secondary MH formation begins. This is marked by an increase in the slope of these curves, and a corresponding localized (and short-term) increase in the F_A value. These observations are obvious in the first cooling step.

The experimental results show temperature upticks in subsequent cooling steps, and these are also captured by the simulation but at a much attenuated level that is not discernible in Figs. 10 and 11. The small step-wise changes in the boundary temperature at each step of the long overall cooling process in Case C4 constitute a mild MH formation scenario, so that secondary hydrate formation does not appear to be an issue and the multiple changes in the slopes of the variables in Fig. 12 denote the beginning of another cooling step. Note that the numerically-predicted average phase saturations are in good agreement with earlier estimation (see Fig. 8).

4.4.4 Spatial distributions in Cases C1 to C4

A key objective of the study is to determine if it is possible to create relatively homogeneous samples of hydrate-bearing cores, to be used in subsequent dissociation experiments with the belief hypothesis that homogeneity of the samples leads to more reliable conclusion and results. This being the case, in this section we focus on the various distributions in the cores at the end of the MH formation process.

Fig. 13 presents the simulated spatial distributions of P, T, S_H, S_A and S_G at the end of the hydrate formation process in Cases C1 to C4. The final pressures are practically uniform (see Fig. 13a) at P = ~3.1 MPa in all cases. This is attributed to the large permeability of the sandy core (k = 3.83 darcys) and the relatively small volume of the reactor (V = 1.0 L). Conversely, the temperature distributions (Fig. 13b exhibit very significant spatial variations along the height of the reactor. There is a warm region at the top of the reactor (the site of the insulated release valve) that increases in temperature (from about 3.5 ^{o}C to 5.0 ^{o}C) and extent/footprint as we move from Case C1 to Case C4, and a cold region at the bottom of the reactor that is in contact with the circulating cooling water, where the temperature varies between 0.8 and about 1.0 ^{o}C. Inspection of the T-distribution in the cores at the end of the four experiments clearly indicates the effect of the obviously imperfect insulation of the top of the reactor. Despite our best efforts and the use of the best possible materials, there are significant heat inflows from the surroundings that increase as the number of the cooling steps and, consequently, the duration of the experiments increases. Thus, the average temperature in the cores (listed in white numbers at the bottom of panels b1 to b4 in Figure 13b) increase consistently from Case 1 to Case 4 (1.5 ^{o}C in C1 < 1.6 ^{o}C in C2 < 1.8 ^{o}C in C3 < 2.5 ^{o}C in C4), as does the temperature at the reactor top, with Case C4 exhibiting the highest temperature.

As expected, the significant heterogeneity in temperature is expected to be associated with similar heterogeneity in the phase saturations. This is evident in Figs. 13c, 13d and 13e, in which heterogeneity in S_H, S_A and S_G, respectively, increases from Case C1 (the least heterogeneous) to Case C4, which shows tremendous heterogeneity. The general trends – common to all cases – of (a) MH accumulating near the reactor bottom (Fig. 13c, with maximum S_H increasing from 0.36 in Case C1 to 0.98 in Case C4) where the temperature is at its lowest because of the vicinity to the cooling boundary, (b) gas accumulating near the top (Fig. 13e) because of buoyancy and higher T and (c) S_A decreasing as S_H increases, conform to expectations. Note that despite the significant

spatial variation in the phase saturations, their average values (denoted by with white letters and numbers at the top of the panels in Fig. 13) are remarkably similar.

The obvious conclusions from the qualitative review of Fig. 13 are that, *with the current design of the experimental apparatus, which reflects the standard in laboratory investigations involving the excess-water MH-forming process*: (a) the original assumption that multiple cooling steps and a longer MH formation process would lead to improved homogeneity of the hydrate-bearing cores is invalid because of insulation imperfections, (b) contrary to expectations, the fastest cooling produces the least heterogeneous sample, and (c) it is not possible to produce homogeneous samples.

4.4.5 Quantifying the level of heterogeneity

In addition to the visual and qualitative determination of heterogeneity discussed in the previous section, we quantified the spatial distribution of the difference between the simulated and the average S_H (Fig. 14) by estimating two types of norms (σ_2 and σ_{inf} corresponding to the norm 2 and the norm of infinity) using the following equations

$$\sigma_2 = \left(\sum_{i=1}^{n} \left[\rho_H V_i \phi (S_i - S_{avg}) \right]^2 \right)^{1/2} \tag{11}$$

$$\sigma_{\inf} = \max_i \left| S_i - S_{avg} \right| \tag{12}$$

where S_i represents the S_H, and V_i represents the volume of the i^{th} element of the reactor domain. The results of the application of Eqs. 11 and 12 indicate that the degree of spatial heterogeneity follows consistently the order C4 > C2 > C3 > C1, as the values of σ_2 (4.03 > 1.88 > 1.61 > 0.59) and σ_{inf} (0.66 > 0.31 > 0.29 > 0.15) clearly reveal. These results provide a quantitative basis to strengthen the conclusions reached in Section 4.4.4. As suggested by the qualitative visual inspection of Fig. 13, the single-step fast cooling in Case C1 yielded the least heterogeneous uniform (but far from acceptably homogeneous) distribution. Cases C2 and C3 exhibit similar level of heterogeneity, but more pronounced than in C1. Case C4, with the most number of cooling steps and the longest formation time, resulted in the highest level of heterogeneity. Similar behaviour was reported recently in studies involving X-ray CT [59] and MRI scans [60] that visualized the in-situ phase distribution.

4.5 Effect of insulated boundary on the uniformity of S_H

In the analysis of the results n Cases C1 to C4, the failure to produce homogeneous cores appeared to be caused by the imperfect insulation of the top of the apparatus despite efforts to minimize heat inflows through it. This conclusion was indicated by the evolution of T in the reactor. We attempted to conclusively determine that heat inflows were indeed the reason for the observed persistent spatial heterogeneities of T and the saturations of the various phases in Cases C1 to C4. Thus, we investigated by means of numerical simulation the spatial distributions of these key variables in the cores in four Cases (C1I to C4I) that differed from the original C1 to C4 cases only in that the reactor top was completely insulated ─ by setting the relevant thermal conductivity to zero.

Fig. 15 shows the spatial distributions of T, S_H, S_A, S_G and ΔS_H in Cases C1I to C4I at the end of their respective cooling process. P is practically uniform in all cases and is not shown here. A general comment is that the spatial uniformity of all the key variables has improved significantly over that in Cases C1 to C4. The spatial variations of T in Fig 15a are much smaller and decrease consistently as we move from Case C1I to Case C4I because more time is available for heat equilibration and stabilization as the cooling period increases. The same pattern is observed in the spatial distributions of S_H, S_A and S_G (Figs. 15b, 15c and 15d, respectively): they are much more uniform than that in Cases C1 to C4 (see Fig. 13), the uniformity increases with the number of cooling steps, and the most homogeneous distributions (but far from complete uniformity) occur in Case C4I. Thus, S_H in that case varies from a minimum $S_H = 0.29$ near the centre to maximum of $S_H = 0.37$ in the vicinity of the reactor lower boundary with an average $S_H = 0.33$, while in Case C1I S_H varies between 0.25 and 0.40. The variations in S_G follow the same pattern, but the S_A distribution is generally more uniform.

These results support the original hypothesis that a longer cooling period and a slow hydrate formation rate would result in a more uniform core, provided the reactor top is perfectly insulated (a requirement not met in the actual experiments C1 to C4). However, perfect uniformity is still elusive, and it is reasonable to expect that it is not even possible given the fact that heat exchange between the core and its surroundings cannot be instantaneous. It is expected that even more uniform distributions can be achieved if a new apparatus design is involved, in which the circulating water bath (i.e., the temperature boundary) covers the entire reactor and not just its lower part as was the case here.

5. Summary and conclusions

The examination of hydrate cores under laboratory conditions provides insights into the hydrate properties and overall behaviour during formation and dissociation [14]. A persistent issue in artificial samples is the spatial heterogeneity of hydrate in the core [15, 20, 24, 26], as there is evidence that it can affect the production behaviour exhibited during laboratory experiments of dissociation [26]. In the absence of direct visualization capabilities, numerical simulation predictions of the hydrate distribution are the only means of addressing the issue of heterogeneity [33, 34, 36]. A reasonable assumption is that the addition of the complexity of spatial heterogeneity to the coupled (and complex) processes of fluid and heat flow during hydrate formation in laboratory cores may lead to potentially significantly different results, thus increasing the uncertainty about the reliability of the numerical predictions of the system behaviour. Consequently, creating and working with more homogeneous samples is desirable, as the underlying hypothesis is that it is expected to lead to more reliable conclusions about the hydrate system behaviour.

This study investigates the possibility of creating spatially homogeneous samples using a specific technique (excess-water), and the conditions under which this may be likely or even feasible. Four different cooling regimes are designed to induce MH formation in a sandy medium with a detailed analysis on the dynamic behaviour of MH formation. The phase saturations of all phases are estimated based on a pore-volume balance method and the spatial distributions of S_H are predicted by numerical simulations following the approach of Yin et al. [33] in all experiments. Our findings offer explanations for the formation of MH at preferential locations and shed light on other new techniques or reactor designs (with different cooling locations) to form representative homogeneous MH samples.

The following conclusions can be drawn from this study:

(1) With the current design of the experimental apparatus, which reflects the standard in laboratory investigations involving the excess-water MH-forming process,

(a) the final average phase saturations in the cores are very similar (despite significant differences in the number of cooling steps and the duration of the cooling process) when the initial and the final *P* and *T* are the same,

(b) the original assumption that multiple cooling steps and a longer MH formation process would lead to improved homogeneity of the hydrate-bearing cores is invalid because of heat inflows caused by insulation imperfections, and,

(c) contrary to expectations, the fastest cooling process produces the least heterogeneous samples, with very high hydrate concentration near the bottom of the core.

(2) An improved design of the experimental apparatus that completely eliminates heat exchanges with its surrounding through a perfect insulation

(a) leads to improved (but still imperfect) homogeneity of the phase saturation distributions in the cores,

(b) contrary to the observations in the standard apparatus design case, the uniformity of phase saturation distributions increases with the length of the cooling period because of a more desirable heat exchange regime, and

(c) even better uniformity of phase saturation distributions would be expected if the apparatus design involves a circulating water (constant temperature) boundary surrounding the entire reactor

Producing perfectly homogeneous samples is an elusive (and probably impossible) task because of the realities of the continuous heat transfer between the core and its surroundings.

Acknowledgement

The financial support from the National University of Singapore (R-261-508-001-646 and R-261-508-001-733) is greatly appreciated. Dr. George Moridis, the holder of the ExxonMobil Visiting Chair in the Department of Chemical and Biomolecular Engineering at NUS, extends his thanks to ExxonMobil and NUS for their support. Zhenyuan Yin would like to thank the IPP scholarship sponsored by LRSPL and EDB.

Tables

Table 1. A list of the types of the sensors used in the study with location and accuracy.

Sensor Name	Type	Location	Accuracy
T_{a1}-T_{a6}	Temperature sensor	r = 25.0 cm (see Fig. 1b)	± 0.1 ^{o}C
T_{b1}-T_{b6}	Temperature sensor	r = 38.0 cm (see Fig. 1b)	± 0.1 ^{o}C
T_{bath}	Temperature sensor	Water Bath	± 0.1 ^{o}C
P_{top} and P_{bot}	Pressure sensor	Top and bottom of reactor (see Fig. 1a)	± 20.0 kPa

Table 2. Thermophysical properties of sandy medium, reactor materials, parameters of constitutive models and boundary conditions

Parameter	Value
Gas composition	100% CH_4
Hydration number (N_H)	6.0
Absolute permeability (k)	$k_r = k_z = 3.83 \times 10^{-12}$ m^2
Porosity of sandy medium (ϕ)	0.448
Density of quartz sand (ρ_s)	2650 kg/m^3
Density of SS316 (ρ_{ss})	8000 kg/m^3
Thermal conductivity of sand under dry condition ($k_{\theta d}$)	1.20 W/(m ºC)
Specific heat of quartz sand (C_R)	800 J/(kg ºC)
Thermal conductivity of SS316 ($k_{\theta S}$)	16.0 W/(m ºC)
Specific heat of SS316 (C_S)	500 J/(kg ºC)
Thermal conductivity of water (k_{water})	0.60 W/(m ºC)
Thermal conductivity of air (k_{air})	0.024 W/(m ºC)
Water boundary temperature (T_{bath})	see Fig. 6
Ambient boundary temperature (T_{air})	20.0 ºC
Composite thermal conductivity model (k_θ) [49]	$k_\theta = k_{\theta d} + \phi(k_{\theta A} S_A + k_{\theta H} S_H + k_{\theta G} S_G)$
Relative permeability model (Stone's model [52])	$k_{rA} = (\frac{S_A - S_{irA}}{1 - S_{irA}})^{n_A}$
	$k_{rG} = (\frac{S_G - S_{irG}}{1 - S_{irG}})^{n_G}$
n_A	3.0
n_G	3.0
S_{irA}	0.10
S_{irG}	0.01
Capillary pressure model (vG model [44])	$P_{cap} = -P_0[(S^*)^{-1/\lambda} - 1]^{1-\lambda}$
	$S^* = \frac{S_A - S_{irA}}{S_{mxA} - S_{irA}}$
S_{irA}	0.099
λ	0.60
P_0	2000 Pa
S_{mxA}	1.00
Hydrate reaction kinetic model (Kim et al. [53])	$n_H = F_A K_0 A_S \exp(\frac{-\Delta E}{RT})(f_{eq} - f_g)$
Hydration reaction constant (K_0)	3.6×10^4 mol/(m^2 Pa s)
Activation energy (ΔE)	81.0 kJ/mol
Reaction surface area (A_S)	Moridis [49]
Surface area adjustment factor (F_A)	(see Table 3) following Yin et al. [33]

Table 3. Summary of the initial conditions for MH formation with supersaturation, sub-cooling, induction time, growth time, methane conversion to hydrate, and average phase saturations in reactor [a].

Exp. No.	**Cooling Step**	**Super-saturation**	**Sub-cooling (°C)**	**Cooling rate (°C/min)**	T_{peak} **(°C)**	t_{ind} **(min)**	**Initial** n_{CH4} **(mol)**	**Initial** n_{H2O} **(mol)**	**Initial** S_A	**Initial** S_G	**Growth time (hr)**	x_{CH4} (%)	S_H	S_A	S_G
C1	1	2.4	11.0	0.21	2.0	58.2	1.32	9.67	0.40	0.60	10.0	74.3	0.31	0.15	0.54
C2	1	0.9	4.0	0.14	1.5	84.0	1.32	9.72			8.1	44.7	0.19	0.25	0.56
	2	–	–	0.17	–	–					5.1	75.0	0.31	0.15	0.54
C3	1	0.6	2.0	0.10	0.3	105.6	1.32	9.67			7.2	38.9	0.12	0.30	0.58
	2	–	–	0.27	–	–					6.0	60.6	0.25	0.20	0.55
	3	–	–	0.14	–	–					16.5	73.4	0.31	0.15	0.54
C4	12	–	–	0.02	–	–	1.32	9.70			300.0	74.1	0.32	0.16	0.52

[a] The initial experimental temperature was T = 16 °C and the pressure was P = 9.5 MPa for all the experiments.

Table 4. Summary of the optimized values of F_A in this study.

Simulation Case No.	t_{start} **(hr)**	t_{end} **(hr)**	F_A
C1	0.0	2.0	0.2
	2.0	8.0	0.03
	8.0	11.0	0.1
C2	0.0	1.5	0.05
	1.5	2.5	0.15
	2.5	6.0	0.03
	6.0	8.0	0.15
	8.0	13.0	0.05
C3	0.0	8.0	0.06
	8.0	11.5	0.03
	11.5	13.1	0.16
	13.1	29.5	0.012
C4	0	300.0	0.022

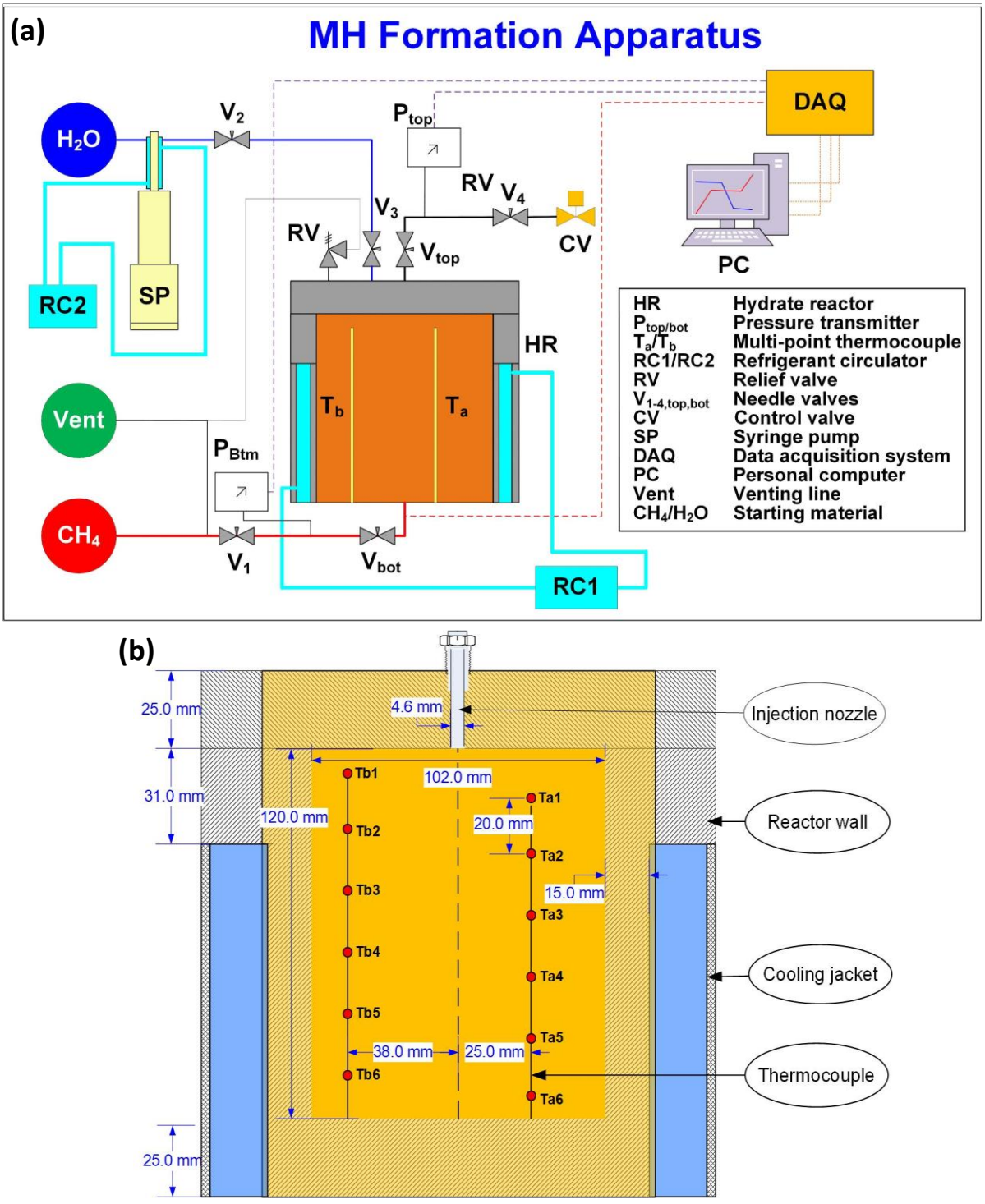

Figure 1. Schematics of (a) experimental apparatus and of (b) cross-section view of the cylindrical reactor showing the locations of the cooling jacket, the two multi-point thermocouples and the water injection nozzle.

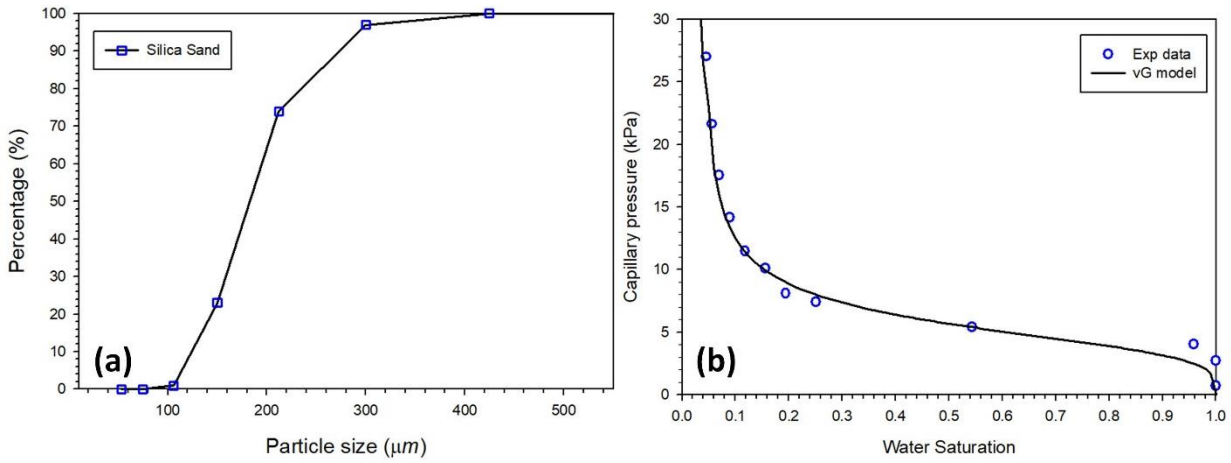

Figure 2. (a) Particle size analysis of the sand sample; and (b) the measured capillary pressure against water saturation with the fitted curve using vG model.

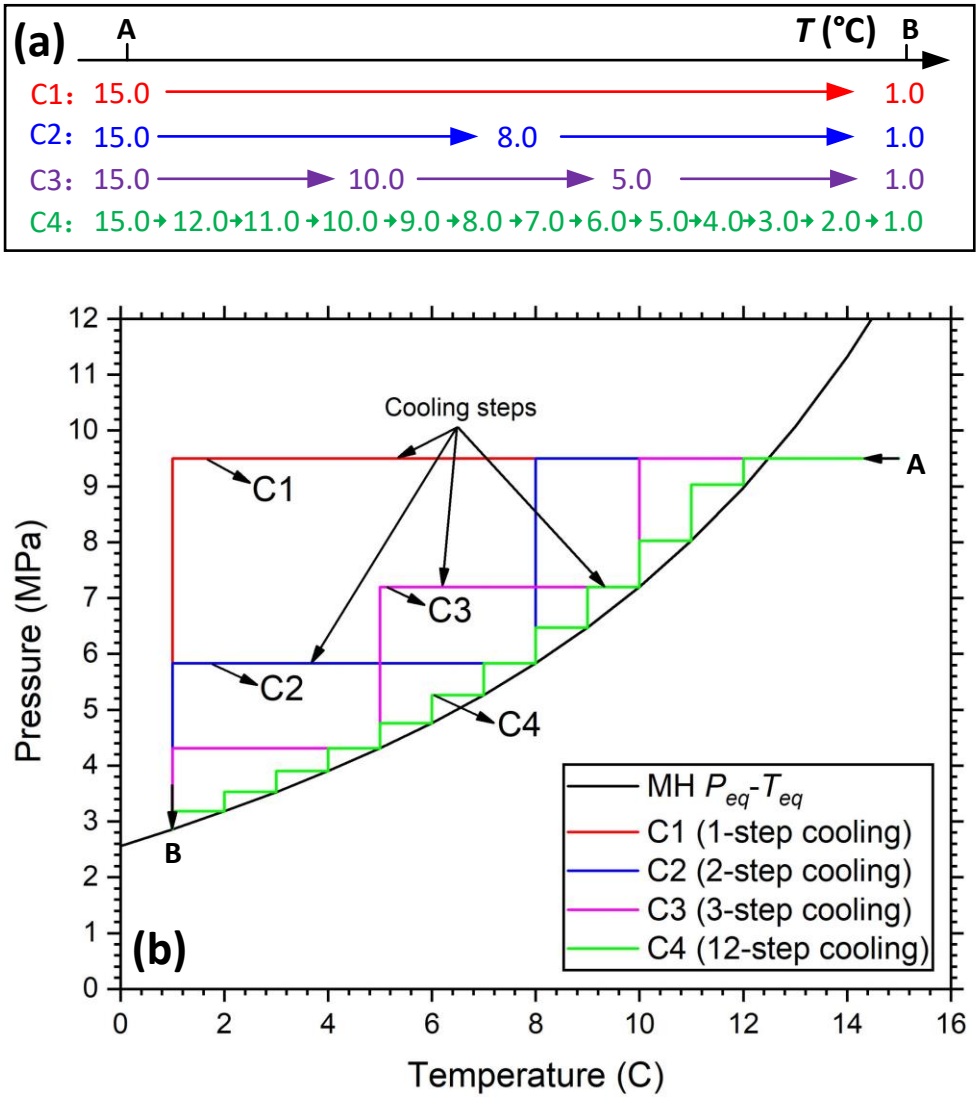

Figure 3. Schematics of (a) the four different multi-stage cooling regimes used in the MH formation experiments labelled as C1 = 1-stage cooling, C2 = 2-stage cooling, C3 = 3-stage cooling and C4 = 12-stage cooling; and (b) the trajectory of *P*-*T* during MH formation in relationship to the MH P_{eq}-T_{eq} curve.

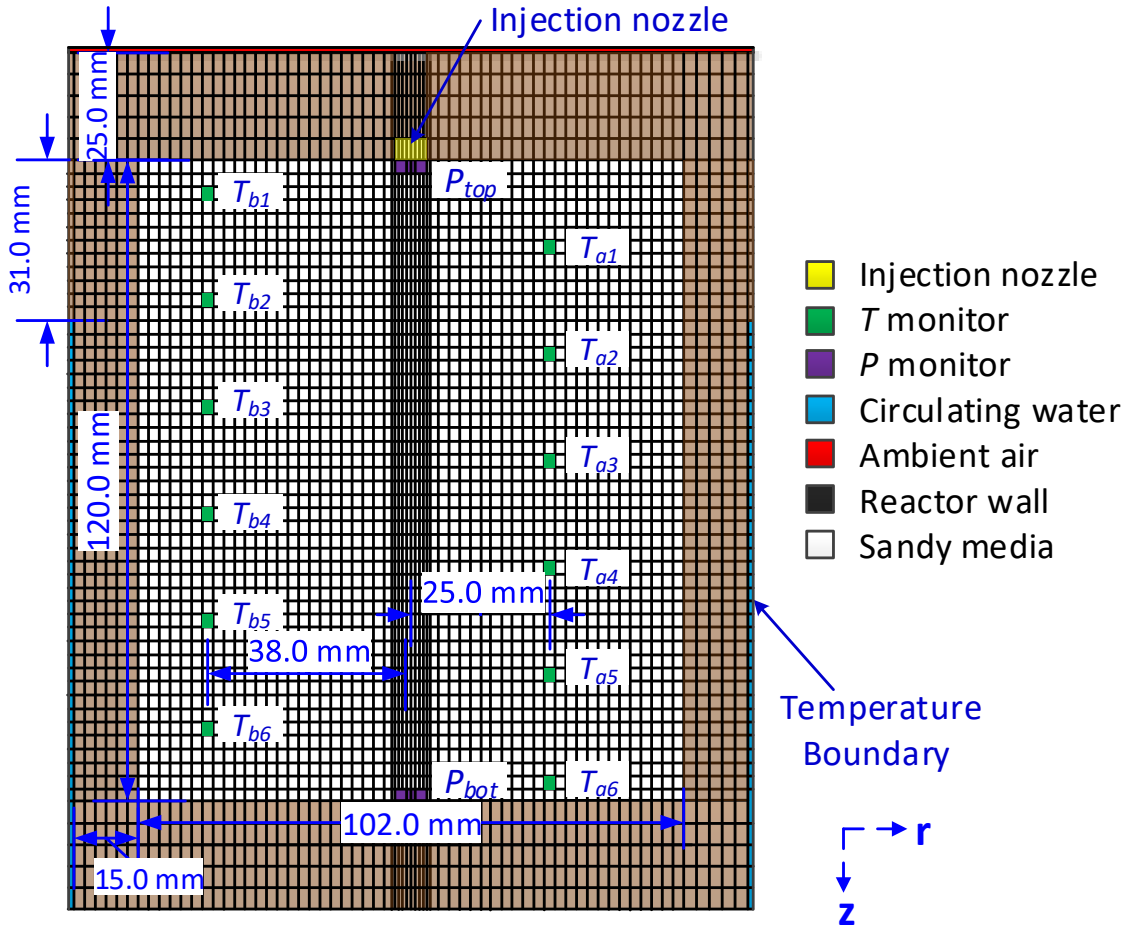

Figure 4. A schematic of the grid of the simulation domain used in the numerical study.

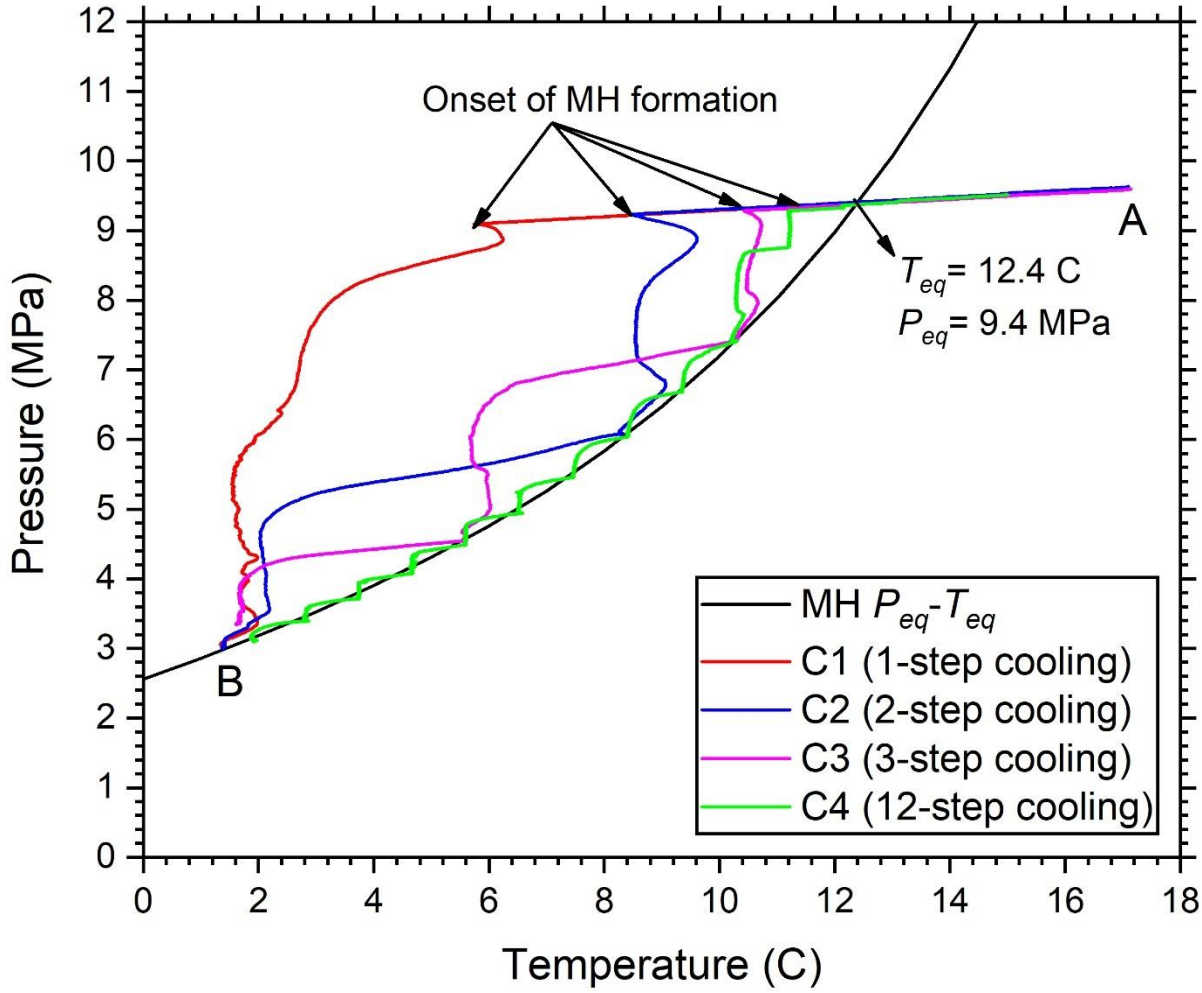

Figure 5. The trajectory of experimental measured P_{avg}-T_{avg} in all four experiments in relation to the MH equilibrium curve.

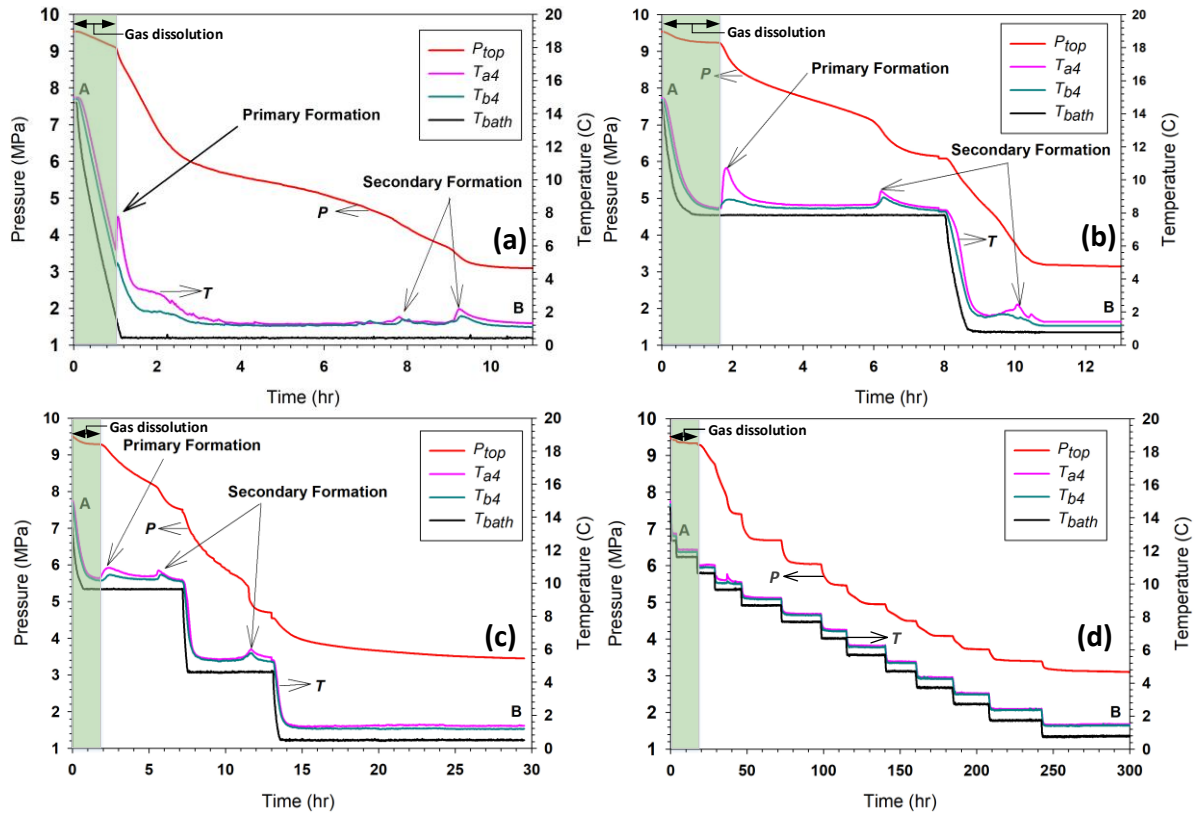

Figure 6. Evolution of P (P_{top} refers to the location of the pressure sensor, see Fig. 1a) and T (T_{a4} and T_{b4} refer to the location of the temperature sensors see Fig. 1b, T_{bath} refers to the location of the circulating water bath) over time in four different cooling regimes (a) C1, (b) C2, (c) C3, and (d) C4 (gas dissolution until onset of hydrate nucleation is shaded in green).

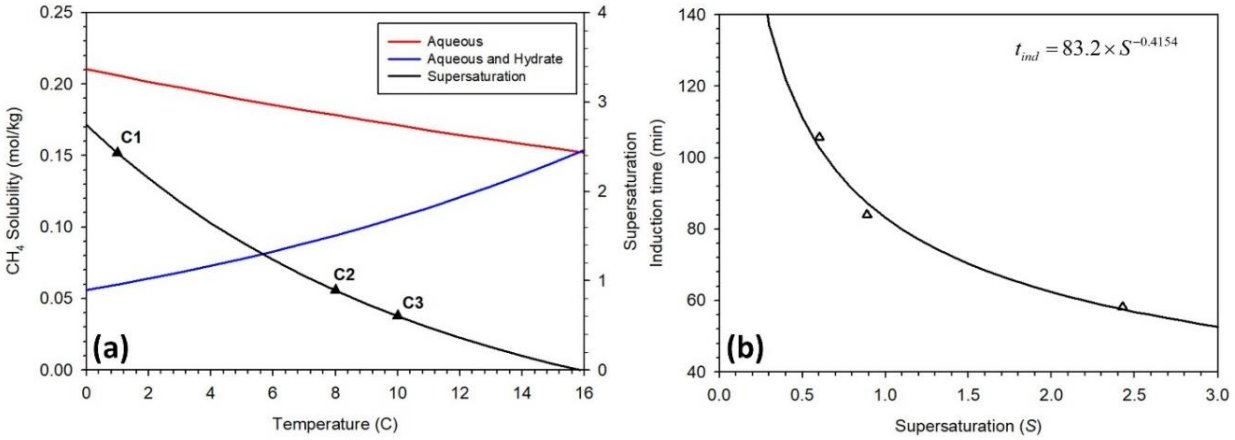

Figure 7. (a) CH_4 solubility in aqueous phase [61] and in aqueous-hydrate equilibrium [45] against temperature at P = 9.2 MPa with calculated S; (b) the relationship between induction time (t_{ind}) and supersaturation (S) with fitted parameters.

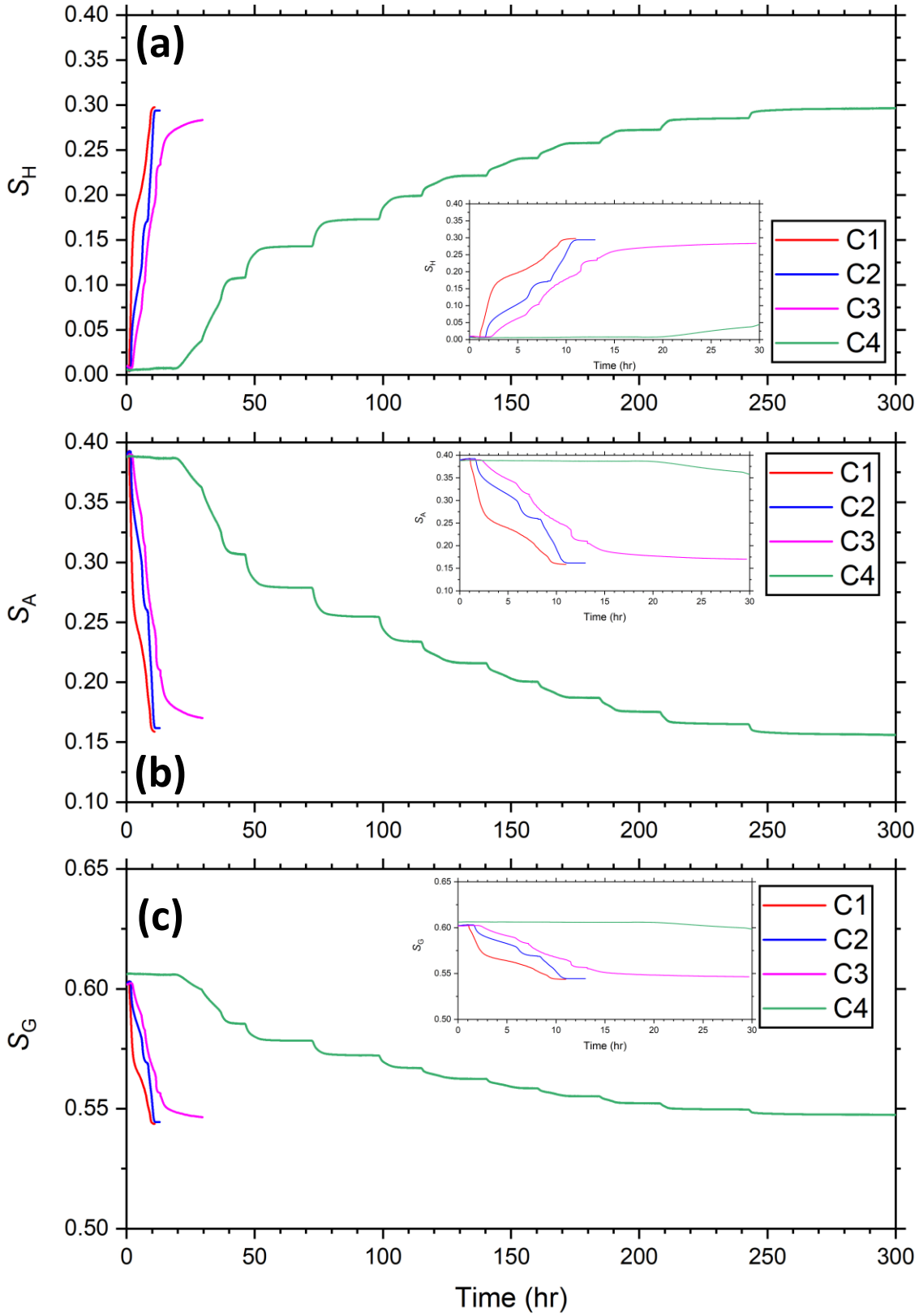

Figure 8. Evolution of the average phase saturations of (a) S_H, (b) S_A and (c) S_G over time for t = 0−300.0 hr in experiments C1-C4 with a zoom-in panel for t = 0−30.0 hr.

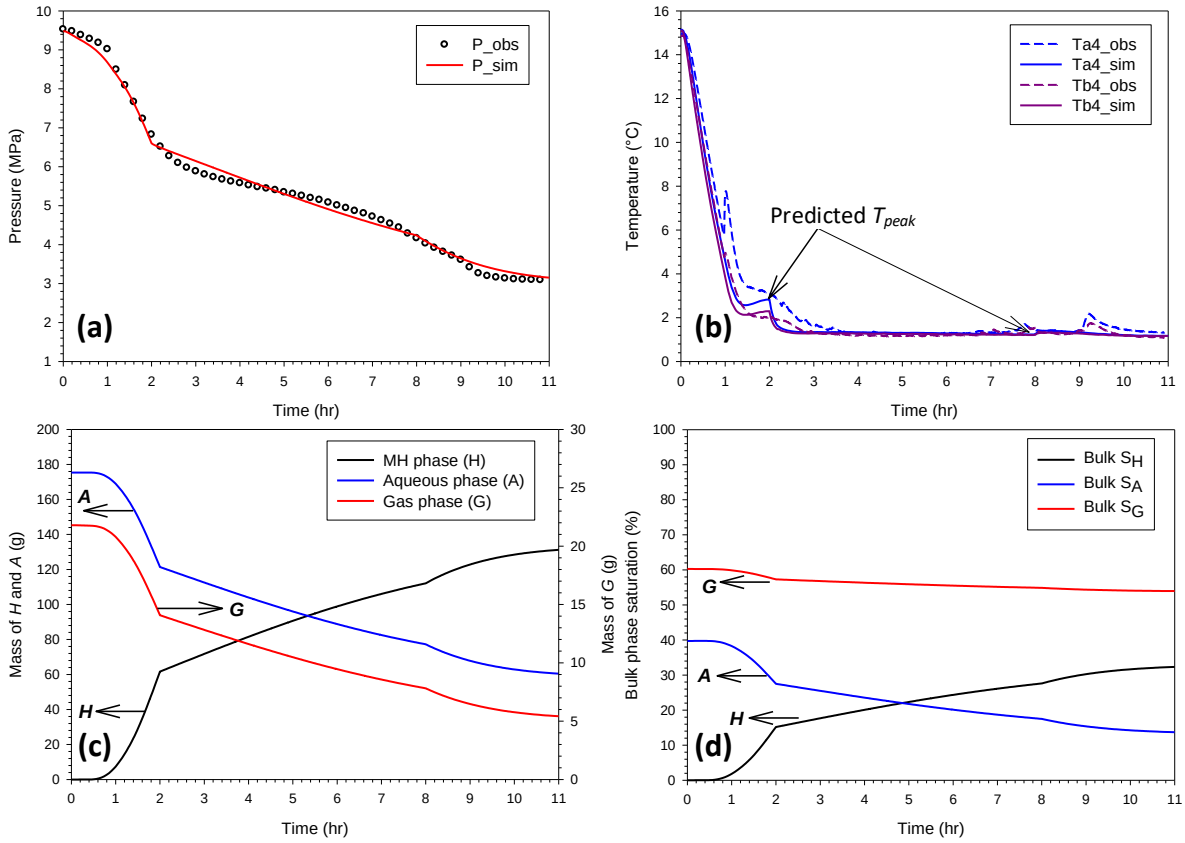

Figure 9. Evolution of (a) pressure, (b) temperature, (c) the mass and (d) the phase saturations of *H*, *A* and *G* over time simulated in Case C1. Experimental measured temperature is shown as dotted line in Fig. 9b to capture the T_{peak}.

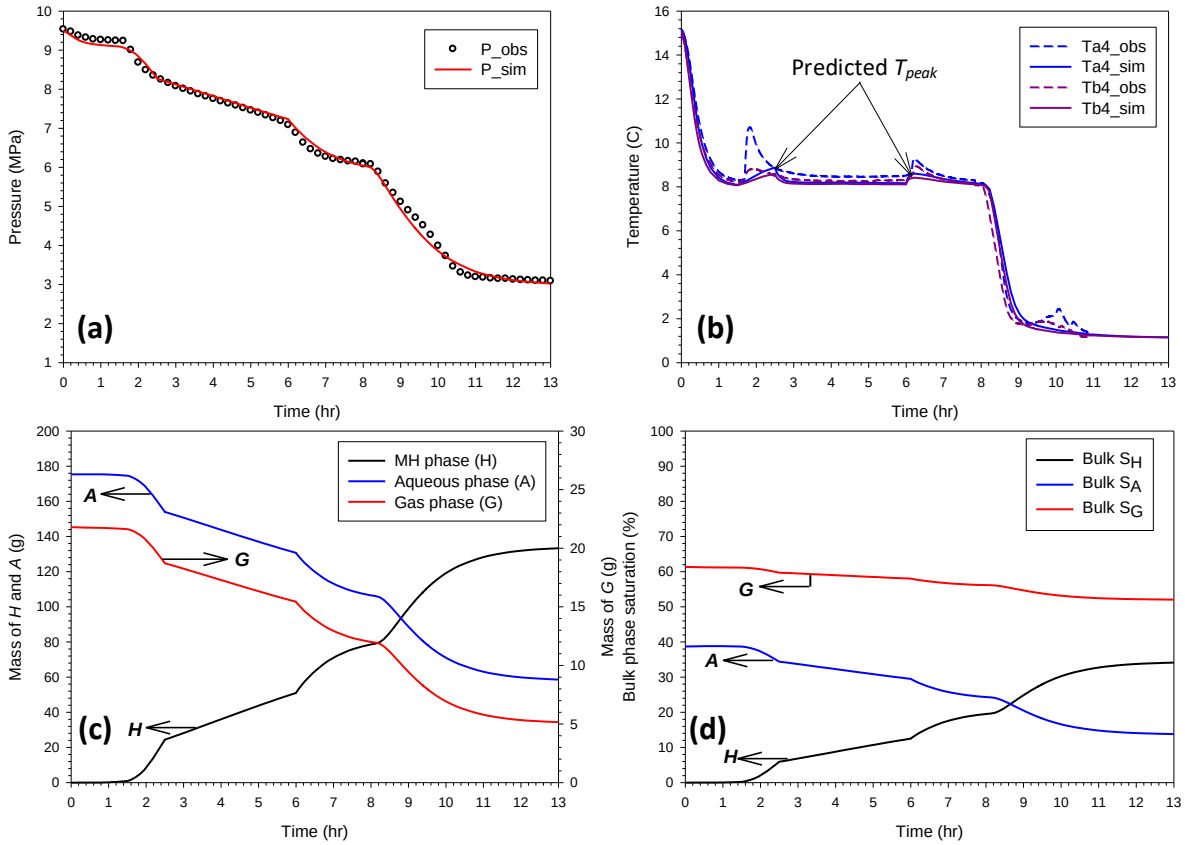

Figure 10. Evolution of (a) pressure, (b) temperature, (c) the mass and (d) the phase saturations of *H*, *A* and *G* over time simulated in Case C2. Experimental measured temperature is shown as dotted line in Fig. 10b to capture the T_{peak}.

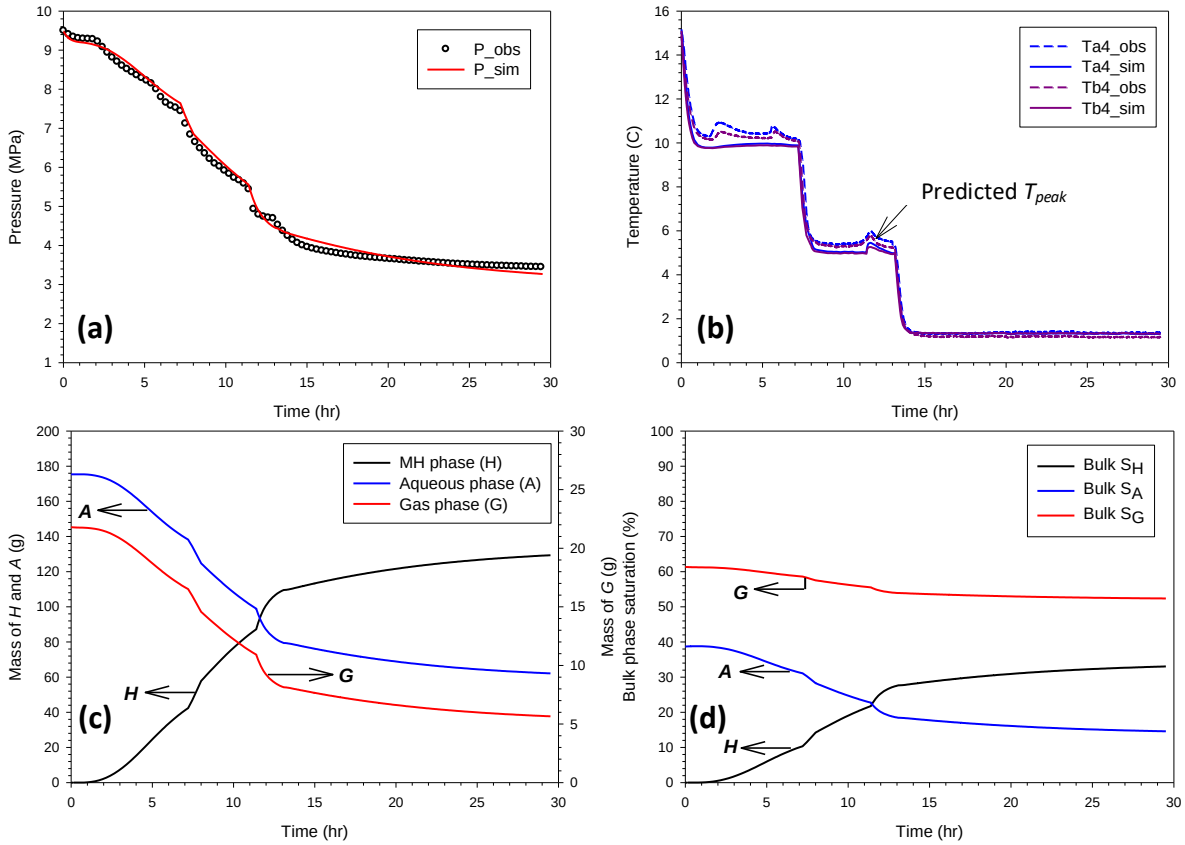

Figure 11. Evolution of (a) pressure, (b) temperature, (c) the mass and (d) the phase saturations of *H*, *A* and *G* over time simulated in Case C3. Experimental measured temperature is shown as dotted line in Fig. 11b to capture the T_{peak}.

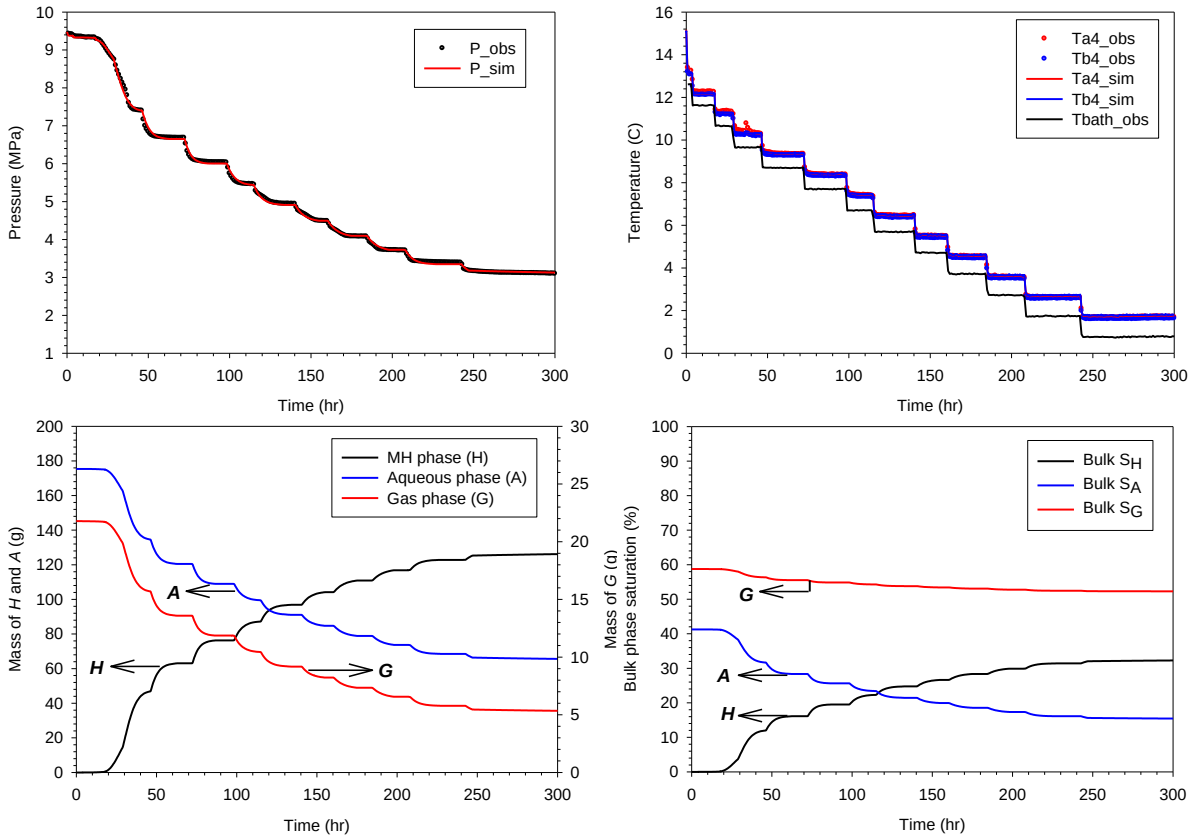

Figure 12. Evolution of (a) pressure, (b) temperature, (c) the mass and (d) the phase saturations of *H*, *A* and *G* over time simulated in Case C4.

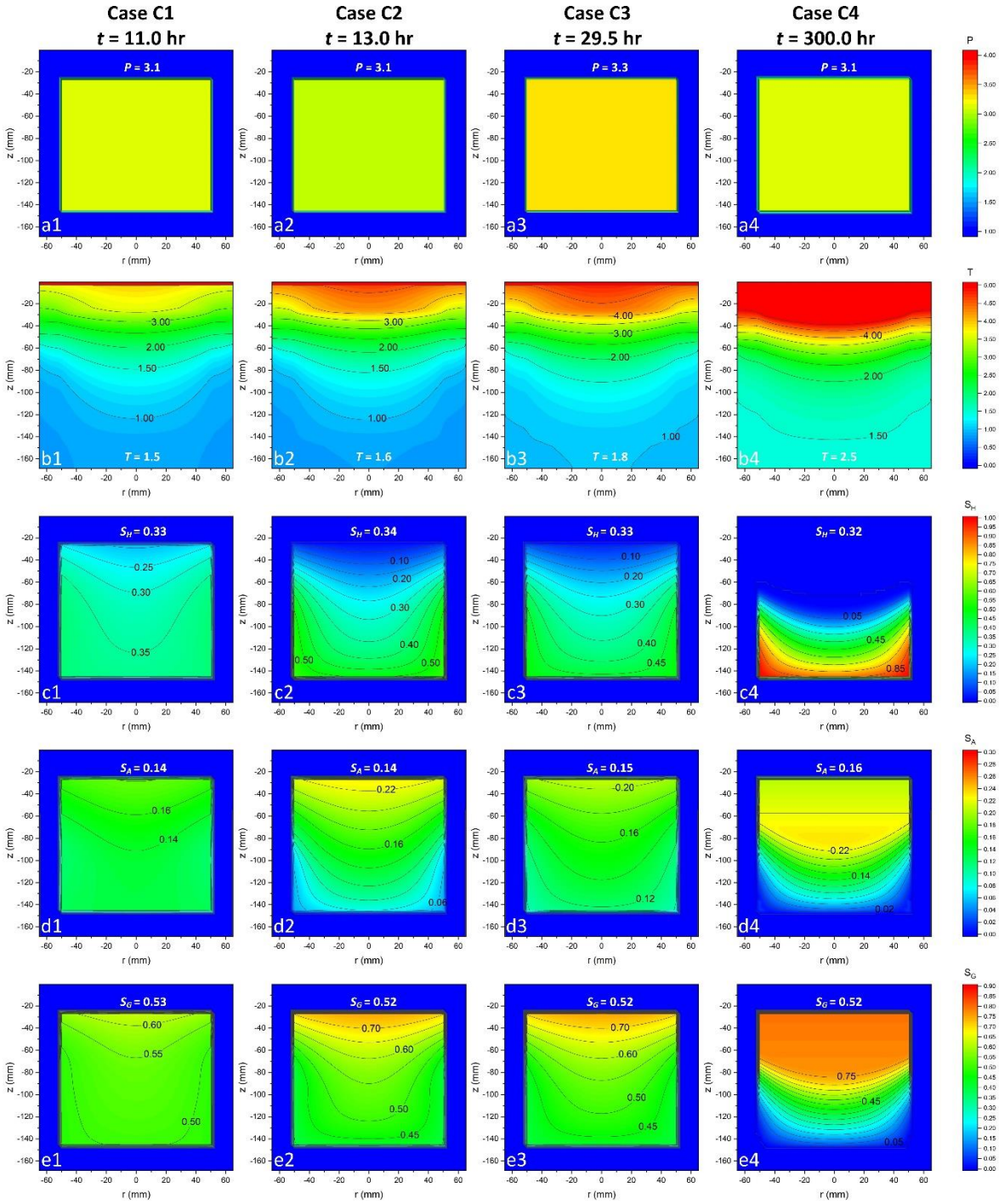

Figure 13. Spatial distributions of P, T, S_H, S_A and S_H derived from numerical simulations at the end of the MH formation processes in Cases C1 to C4 (common scales are to the right of figures). The numbers in white at the top and bottom of the various panels indicate the average values of the depicted variables in the reactor in the four experiments.

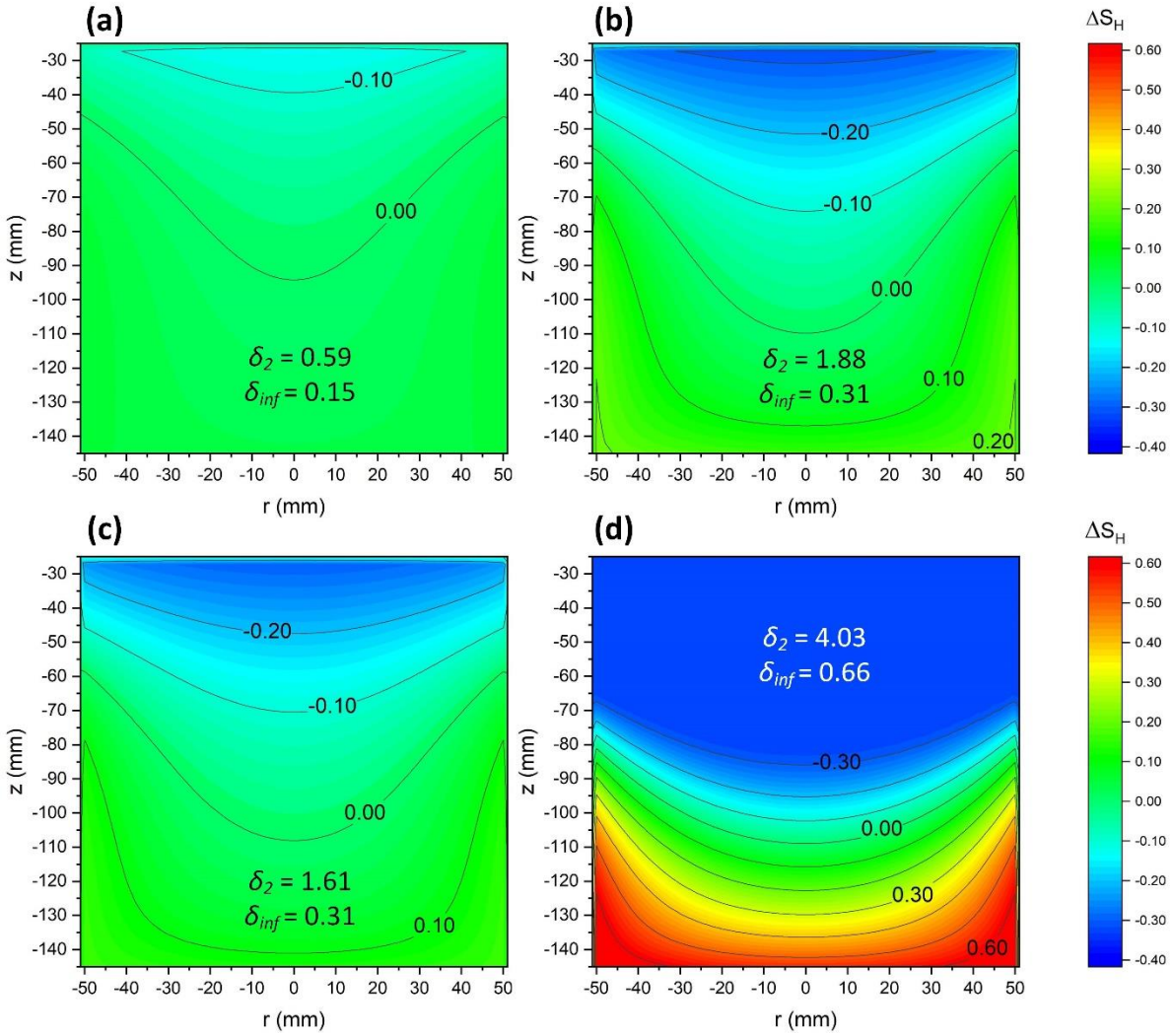

Figure 14. Spatial distributions of ΔS_H (S_H - $S_{H,avg}$) inside reactor in (a) Case C1, (b) Case C2, (c) Case C3 and (d) Case C4 with two types of norms quantifying the degree of spatial heterogeneity.

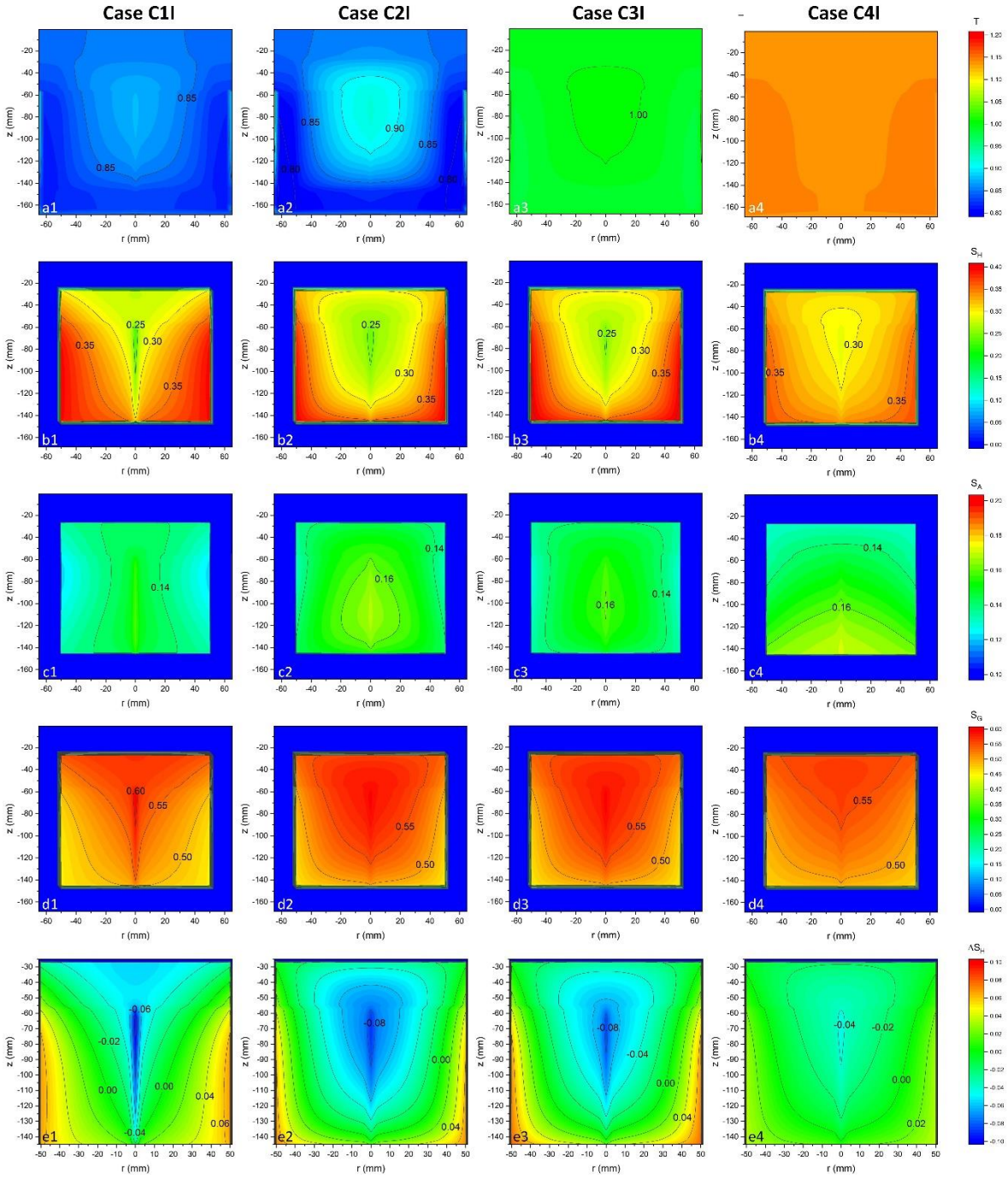

Figure 15. Spatial distributions of (a) T, (b) S_H, (c) S_A and (d) S_G and (e) ΔS_H derived from numerical simulations at the end of the MH formation processes in Cases C1I to C4I (common scales are on the right side of figures).

List of Tables:

List of Figures:

Nomenclature

A subscript	Aqueous phase
A_S	Surface area of hydrate particle
BET	Brunauer-Emmett-Teller
c_A	Solubility of CH_4 in aqueous phase
c_{AH}	Solubility of CH_4 in aqueous-hydrate equilibrium
CT	Computer tomography
D	Thickness
D	Diameter
DSC	Differential calorimetry scanning
ERT	Electrical resistivity tomography
ΔE	activation energy
F_A	Surface area adjustment factor
f_g	Fugacity of CH_4 in gas phase
f_{eq}	Fugacity of CH_4 at hydrate equilibrium
Δf	Fugacity difference
G subscript	Gas phase
H	Height
H subscript	Hydrate phase
HBS	Hydrate bearing sediment
k	Absolute permeability
K	MH formation reaction rate constant
MH	Methane hydrates
MRI	Magnetic resonance imaging
N	Number of moles
N_H	Hydration number
P	Pressure
P_{avg}	Average pressure from monitoring sensors
P_{bot}	Pressure at bottom position
P_{eq}	MH equilibrium pressure
P_{top}	Pressure at top position
Q_G	Rate of gas injection
Q_W	Rate of water injection
r	Radial direction
R	Radius
S	Supersaturation
S_{avg}	Average phase saturation
S_i	Phase saturation of the i^{th} phase
S_A	Phase saturation of A
S_G	Phase saturation of G
S_H	Phase saturation of H
STP	Standard temperature and pressure (0 ^oC and 1 atm)
t	time
t_{ind}	Induction time
T	Temperature
TCM	Trillion cubic meters

T_{avg}	Average temperature from monitoring sensors
T_{eq}	MH equilibrium temperature
T_{peak}	Peak temperature observed during MH formation
T_w	Temperature of water bath
T+H	TOUGH+Hydrate
ΔT_{sub}	Degree of sub-cooling
vG	van-Genuchten
V	Volume
z	Vertical direction
ρ	Molar density
σ_2	Norm-2
σ_{inf}	Norm of infinity
ϕ	Porosity

References

[1] Sloan ED, Jr., Koh CA. Clathrate Hydrates of the Natural Gases. 3rd ed. Boca Raton, FL: CRC Press; 2008.
[2] Boswell R, Collett TS. Current Perspectives on Gas Hydrate Resources. Energy & Environmental Science. 2011;4:1206-15.
[3] BP. BP Statistical Review of World Energy. Natural gas2017. p. 26.
[4] Milkov AV. Global estimates of hydrate-bound gas in marine sediments: how much is really out there? Earth-Science Reviews. 2004;66:183-97.
[5] Oyama A, Masutani MS. A Review of the Methane Hydrate Program in Japan. Energies. 2017;10.
[6] Xinhua. China wraps up combustible ice mining trial, setting world records. Guang Zhou2017.
[7] Babu P, Yee D, Linga P, Palmer A, Khoo BC, Tan TS, et al. Morphology of Methane Hydrate Formation in Porous Media. Energy & Fuels. 2013;27:3364-72.
[8] B. KP, Kristine H, W. JK, Devinder M. Imaging methane hydrates growth dynamics in porous media using synchrotron X-ray computed microtomography. Geochemistry, Geophysics, Geosystems. 2014;15:4759-68.
[9] Marwen C, Andrzej F, Kathleen S, Frieder E, Michael K, David H, et al. Microstructural evolution of gas hydrates in sedimentary matrices observed with synchrotron X-ray computed tomographic microscopy. Geochemistry, Geophysics, Geosystems. 2015;16:1711-22.
[10] Kneafsey TJ, Lu H, Winters W, Boswell R, Hunter R, Collett TS. Examination of core samples from the Mount Elbert Gas Hydrate Stratigraphic Test Well, Alaska North Slope: Effects of retrieval and preservation. Marine and Petroleum Geology. 2011;28:381-93.
[11] Konno Y, Yoneda J, Egawa K, Ito T, Jin Y, Kida M, et al. Permeability of sediment cores from methane hydrate deposit in the Eastern Nankai Trough. Marine and Petroleum Geology. 2015;66:487-95.
[12] Moridis GJ, Kim J, Reagan MT, Kim S-J. Feasibility of Gas Production from a Gas Hydrate Accumulation at the UBGH2-6 Site of the Ulleung Basin in the Korean East Sea. Journal of Petroleum Science and Engineering. 2013;108S:180-210.
[13] Moridis GJ, Kowalsky MB, Pruess K. Depressurization-induced Gas Production from Class-1 Hydrate Deposits. SPE Reservoir Evaluation & Engineering. 2007;10:458-81.
[14] Yoneda J, Oshima M, Kida M, Kato A, Konno Y, Jin Y, et al. Permeability variation and anisotropy of gas hydrate-bearing pressure-core sediments recovered from the Krishna–Godavari Basin, offshore India. Marine and Petroleum Geology. 2018.

[15] Kneafsey TJ, Tomutsa L, Moridis GJ, Seol Y, Freifeld BM, Taylor CE, et al. Methane Hydrate Formation and Dissociation in a Partially Saturated Core-scale Sand Sample. Journal of Petroleum Science and Engineering. 2007;56:108-26.
[16] Moridis GJ, Collett TS, Boswell R, Kurihara M, Reagan MT, Koh C, et al. Toward Production from Gas hydrates: Current Status, Assessment of Resources, and Simulation-based Evaluation of Technology and Potential. SPE Reservoir Evaluation & Engineering. 2009;12:745-71.
[17] Yamamoto K. Overview and introduction: Pressure core-sampling and analyses in the 2012–2013 MH21 offshore test of gas production from methane hydrates in the eastern Nankai Trough. Marine and Petroleum Geology. 2015;66:296-309.
[18] Yin Z, Khurana M, Tan HK, Linga P. A review of gas hydrate growth kinetic models. Chemical Engineering Journal. 2018;342:9-29.
[19] Khurana M, Yin Z, Linga P. A Review of Clathrate Hydrate Nucleation. ACS Sustainable Chemistry & Engineering. 2017;5:11176-203.
[20] Linga P, Haligva C, Nam SC, Ripmeester JA, Englezos P. Gas Hydrate Formation in a Variable Volume Bed of Silica Sand Particles. Energy & Fuels. 2009;23:5496-507.
[21] Handa YP, Stupin DY. Thermodynamic properties and dissociation characteristics of methane and propane hydrates in 70-. ANG.-radius silica gel pores. The Journal of Physical Chemistry. 1992;96:8599-603.
[22] Priest JA, Rees EV, Clayton CR. Influence of gas hydrate morphology on the seismic velocities of sands. Journal of Geophysical Research: Solid Earth. 2009;114.
[23] Chong ZR, Yin Z, Tan JHC, Linga P. Experimental investigations on energy recovery from water-saturated hydrate bearing sediments via depressurization approach. Applied Energy. 2017;204:1513-25.
[24] Priegnitz M, Thaler J, Spangenberg E, Schicks JM, Schrötter J, Abendroth S. Characterizing electrical properties and permeability changes of hydrate bearing sediments using ERT data. Geophysical Journal International. 2015;202:1599-612.
[25] Stern LA, Circone S, Kirby SH, Durham WB. Anomalous Preservation of Pure Methane Hydrate at 1 atm. The Journal of Physical Chemistry B. 2001;105:1756-62.
[26] Gupta A, Kneafsey TJ, Moridis GJ, Seol Y, Kowalsky MB, Sloan E. Composite Thermal Conductivity in a Large Heterogeneous Porous Methane Hydrate Sample. The Journal of Physical Chemistry B. 2006;110:16384-92.
[27] Seol Y, Kneafsey TJ. X-ray computed-tomography observations of water flow through anisotropic methane hydrate-bearing sand. Journal of Petroleum Science and Engineering. 2009;66:121-32.

[28] Kneafsey TJ, Rees EVL, Nakagawa S, Kwon T-H. Examination of Hydrate Formation Methods: Trying to Create Representative Samples. LBNL-4845E. Berkeley, California, USA: Lawrence Berkeley National Laboratory; 2010.
[29] Rees EVL, Kneafsey TJ, Seol Y. Methane Hydrate Distribution from Prolonged and Repeated Formation in Natural and Compacted Sand Samples: X-Ray CT Observations. Journal of Geological Research. 2011;2011.
[30] Baldwin BA, Stevens J, Howard JJ, Graue A, Kvamme B, Aspenes E, et al. Using magnetic resonance imaging to monitor CH4 hydrate formation and spontaneous conversion of CH4 hydrate to CO2 hydrate in porous media. Magnetic Resonance Imaging. 2009;27:720-6.
[31] Yang M, Fu Z, Zhao Y, Jiang L, Zhao J, Song Y. Effect of depressurization pressure on methane recovery from hydrate–gas–water bearing sediments. Fuel. 2016;166:419-26.
[32] Priegnitz M, Thaler J, Spangenberg E, Rücker C, Schicks JM. A cylindrical electrical resistivity tomography array for three-dimensional monitoring of hydrate formation and dissociation. Review of Scientific Instruments. 2013;84:104502.
[33] Yin Z, Moridis G, Tan HK, Linga P. Numerical analysis of experimental studies of methane hydrate formation in a sandy porous medium. Applied Energy. 2018;220:681-704.
[34] Yin Z, Moridis G, Chong ZR, Tan HK, Linga P. Numerical analysis of experimental studies of methane hydrate dissociation induced by depressurization in a sandy porous medium. Applied Energy. 2018;230:444-59.
[35] Chong ZR, Pujar GA, Yang M, Linga P. Methane hydrate formation in excess water simulating marine locations and the impact of thermal stimulation on energy recovery. Applied Energy. 2016;177:409-21.
[36] Yin Z, Moridis G, Chong ZR, Tan HK, Linga P. Numerical Analysis of Experiments on Thermally Induced Dissociation of Methane Hydrates in Porous Media. Industrial & Engineering Chemistry Research. 2018;57:5776-91.
[37] Dai S, Seol Y. Water permeability in hydrate-bearing sediments: A pore-scale study. Geophysical Research Letters. 2014;41:4176-84.
[38] Li G, Wu D-M, Li X-S, Lv Q-N, Li C, Zhang Y. Experimental measurement and mathematical model of permeability with methane hydrate in quartz sands. Applied Energy. 2017;202:282-92.
[39] Chen X, Verma R, Espinoza DN, Prodanović M. Pore-Scale Determination of Gas Relative Permeability in Hydrate-Bearing Sediments Using X-Ray Computed Micro-Tomography and Lattice Boltzmann Method. Water Resources Research. 2018;54:600-8.
[40] Li B, Li X-S, Li G, Wang Y, Feng J-C. Kinetic Behaviors of Methane Hydrate Formation in Porous Media in Different Hydrate Deposits. Industrial & Engineering Chemistry Research. 2014;53:5464-74.

[41] Jiang G, Wu Q, Zhan J. Effect of cooling rate on methane hydrate formation in media. Fluid Phase Equilibria. 2010;298:225-30.
[42] Zhang P, Wu Q, Mu C. Influence of temperature on methane hydrate formation. Scientific Reports. 2017;7:7904.
[43] Mali GA, Chapoy A, Tohidi B. Investigation into the effect of subcooling on the kinetics of hydrate formation. The Journal of Chemical Thermodynamics. 2018;117:91-6.
[44] Van Genuchten MT. A Closed-form Equation for Predicting the Hydraulic Conductivity of Unsaturated Soils. Soil science society of America journal. 1980;44:892-8.
[45] Servio P, Englezos P. Measurement of Dissolved Methane in Water in Equilibrium with Its Hydrate. Journal of Chemical & Engineering Data. 2002;47:87-90.
[46] Sloan ED. Gas Hydrates: Review of Physical/Chemical Properties. Energy & Fuels. 1998;12:191-6.
[47] Waite WF, Santamarina JC, Cortes DD, Dugan B, Espinoza D, Germaine J, et al. Physical properties of hydrate-bearing sediments. Reviews of geophysics. 2009;47.
[48] Bagherzadeh SA, Moudrakovski IL, Ripmeester JA, Englezos P. Magnetic Resonance Imaging of Gas Hydrate Formation in a Bed of Silica Sand Particles. Energy & Fuels. 2011;25:3083-92.
[49] Moridis GJ. User's manual for the hydrate v1. 5 option of TOUGH+ v1. 5: A code for the simulation of system behavior in hydrate-bearing geologic media. LBNL-6869E. Berkeley, California, USA: Lawrence Berkeley National Laboratory; 2014.
[50] Moridis GJ. User's manual of the TOUGH+ core code v1. 5: A general-purpose simulator of non-isothermal flow and transport through porous and fractured media. LBNL 6871E. Berkeley, California, USA: Lawrence Berkeley National Laboratory; 2014.
[51] Moridis GJ. User's mannual of the MeshMaker v1. 5 code: A mesh generator for domain discretization in simulations of the TOUGH+ and TOUGH2 familes of codes. LBNL 1005134. Berkeley, California, USA: Lawrence Berkeley National Laboratory 2016.
[52] Stone H. Probability Model for Estimating Three-phase Relative Permeability. Journal of Petroleum Technology. 1970;22:214-8.
[53] Kim HC, Bishnoi PR, Heidemann RA, Rizvi SSH. Kinetics of methane hydrate decomposition. Chemical Engineering Science. 1987;42:1645-53.
[54] Clarke M, Bishnoi P. Determination of the intrinsic rate of gas hydrate decomposition using particle size analysis. Annals of the New York Academy of Sciences. 2000;912:556-63.

[55] Thomas LK, Hellums L, Reheis G. A nonlinear automatic history matching technique for reservoir simulation models. Society of Petroleum Engineers Journal. 1972;12:508-14.
[56] Mullin JW. Crystallization: Elsevier; 2001.
[57] Kashchiev D, Firoozabadi A. Induction time in crystallization of gas hydrates. Journal of Crystal Growth. 2003;250:499-515.
[58] Sun X, Mohanty KK. Kinetic Simulation of Methane Hydrate Formation and Dissociation in Porous MSedia. Chemical Engineering Science. 2006;61:3476-95.
[59] Chen X, Espinoza DN. Ostwald ripening changes the pore habit and spatial variability of clathrate hydrate. Fuel. 2018;214:614-22.
[60] Song Y, Zhang L, Lv Q, Yang M, Ling Z, Zhao J. Assessment of gas production from natural gas hydrate using depressurization, thermal stimulation and combined methods. RSC Advances. 2016;6:47357-67.
[61] Fernández-Prini R, Alvarez JL, Harvey AH. Henry's Constants and Vapor–Liquid Distribution Constants for Gaseous Solutes in H2O and D2O at High Temperatures. Journal of Physical and Chemical Reference Data. 2003;32:903-16.